



The improvement of the cavitation resistance of technical surfaces using high power laser pulses

Master Thesis

Study programme:

N2301 Mechanical Engineering

Study branch:

Machines and Equipment Design

Author:

Rhoda Ayorkor Sai

Thesis Supervisors:

Ing. Miloš Müller, Ph.D.

Department of Power Engineering Equipment





Master Thesis Assignment Form

The improvement of the cavitation resistance of technical surfaces using high power laser pulses

Name and surname: **Rhoda Ayorkor Sai**
Identification number: S18000382
Study programme: N2301 Mechanical Engineering
Study branch: Machines and Equipment Design
Assigning department: Department of Power Engineering Equipment
Academic year: **2019/2020**

Rules for Elaboration:

- A research of processes dedicated for the improvement of the cavitation resistance of technical surfaces with a special focus to the laser shock peening process
- Parameters used to evaluate the improvement of the strength of the treated material surface
- The assembly of an experimental setup for the cavitation resistance testing
- The preparation of samples using the laser shock peening method
- The measurement of cavitation erosion resistance for selected samples
- The evaluation of measurements results and recommendations for the application of the modification process

Scope of Graphic Work: 10
Scope of Report: 50
Thesis Form: printed/electronic
Thesis Language: English



List of Specialised Literature:

1. KIM, Ki-Han, Georges CHAHINE, Jean-Pierre FRANC a Ayat KARIMI. *Advanced experimental and numerical techniques for cavitation erosion prediction*. Dordrecht: Springer, [2014]. Fluid mechanics and its applications, v. 106.
2. FRANC, Jean-Pierre a Jean-Marie MICHEL. *Fundamentals of cavitation*. Boston: Kluwer Academic Publishers, c2004. ISBN 1402022328.
3. BRENNEN, Christopher E. *Cavitation and bubble dynamics*. New York: Cambridge University Press, c2014. ISBN 978-1-107-64476-2.
4. TAKATA, Tomoki, Manabu ENOKI, Pornthep CHIVAVIBUL, Akinori MATSUI a Yuji KOBAYASHI. *Effect of Confinement Layer on Laser Ablation and Cavitation Bubble During Laser Shock Peening*. MATERIALS TRANSACTIONS. 2016, 57(10), 1776-1783.
5. SOYAMA, Hitoshi. *Key Factors and Applications of Cavitation Peening*. Int. Journ. of Peening Science and Technology. 2018, 1(1), 3-60.

Thesis Supervisors: Ing. Miloš Müller, Ph.D.
Department of Power Engineering Equipment

Date of Thesis Assignment: November 1, 2019

Date of Thesis Submission: April 30, 2021

prof. Dr. Ing. Petr Lenfeld
Dean

L.S.

doc. Ing. Petra Dančová, Ph.D.
Head of Department

Declaration

I hereby certify, I, myself, have written my master thesis as an original and primary work using the literature listed below and consulting it with my thesis supervisor and my thesis counsellor.

I acknowledge that my bachelor master thesis is fully governed by Act No. 121/2000 Coll., the Copyright Act, in particular Article 60 – School Work.

I acknowledge that the Technical University of Liberec does not infringe my copyrights by using my master thesis for internal purposes of the Technical University of Liberec.

I am aware of my obligation to inform the Technical University of Liberec on having used or granted license to use the results of my master thesis; in such a case the Technical University of Liberec may require reimbursement of the costs incurred for creating the result up to their actual amount.

At the same time, I honestly declare that the text of the printed version of my master thesis is identical with the text of the electronic version uploaded into the IS/STAG.

I acknowledge that the Technical University of Liberec will make my master thesis public in accordance with paragraph 47b of Act No. 111/1998 Coll., on Higher Education Institutions and on Amendment to Other Acts (the Higher Education Act), as amended.

I am aware of the consequences which may under the Higher Education Act result from a breach of this declaration.

June 12, 2020

Rhoda Ayorkor Sai

ABSTRACT

In this study, the effect of laser shock peening treatment on the cavitation erosion resistance of a stainless-steel type used in pump blades was characterized. The goal of the study was to compare and define the better process parameters of the treatment effective in improving the cavitation erosion resistance of the stainless-steel type. An experimental investigation was conducted using the vibratory apparatus with compliance to ASTM G32 standards. Specimens made of stainless steel 304 were treated using different laser pulse density, and beam size with a 50% overlap. Prior to the cavitation erosion test, the incubation time of the samples was estimated from previous tests of similar samples. Each sample was subjected to ultrasonic pressure pulses at different exposure times using a constant amplitude. mass loss was recorded for each

The incubation period was used to characterize the materials impact resistance and the cavitation erosion resistance was achieved using mass loss tests and represented as the reciprocal of the cumulative volume loss rates. The mean depth of penetration was calculated from volume loss and affirmed using the cavitation erosion profile, measured with contact profilometer. The effect of exposure time on the mean depth was analyzed and found to stabilize after significant exposure time. The mean eroded depth was also compared to the compressive residual stress induced during the laser treatment and used quantitatively to describe the cavitation damage of SS304. The correlation between the cavitation erosion resistance and properties of the improved samples was perused. The variation of the cumulative volume loss with exposure time indicated improvement of the materials cavitation erosion resistance. The results of the study hawed that SS304 treated with higher power density depicted the highest erosion resistance whiles SS304 with lower power density showed the highest impact resistance during the incubation period. The summary of the results in the conclusion explains the outcome of the investigation.

Keywords: cavitation, laser shock peening, residual stress, volume loss, cavitation resistance

ACKNOWLEDGMENTS

First, I wish to thank God Almighty for my life and the strength to in every moment. I would like to thank my family especially Timothy Sai and Mary Sai for providing their support and encouragement in all things. I would like to dedicate this work to the memory of my Father, Daniel N.O. Sai whose pimple and upbringing is the essence of m life. I would like to express my gratitude to my supervisor Ing. Milos Muller, Ph.D., whose support, and guidance has helped me throughout this work and whose advise helped directed me away from mistakes. I would also like to extend my gratitude to Ing. Jan Hujer Ph.D for spending time away from his schedule to provide his assistance. I also want to thank the Ministries of Youth and Sport for the Czech Republic for awarding me a government scholarship. I am also grateful to the group from Hilase Centre of Mrs. Danijela Rostohar, especially Mr. Sanin Zulic from HiLASE centre - Institute of Physics of the Czech Republic, who provided samples treated by LSP for the cavitation testing. I would also like to thank the department of material science for assisting and providing means of evaluating the results of the tests. And to all those who worked hand in hand with me make this work successful, a big thank you to. especially Emmanuel N. Ayisi and Feben Huluka. I appreciate the help.

.

TABLE OF CONTENTS

1	Introduction.....	10
1.1	Description Of Cavitation	11
1.2	Classification Of Cavitation.....	13
1.3	Adverse Effects Of Cavitation In Field Applications	15
1.4	Beneficial Effects Of Cavitation In Field Applications	16
2	Current State Of Knowledge.....	18
2.1	Acoustic Cavitation.....	18
2.1.1	Acoustic Bubble Dynamics.....	20
2.1.2	Factors Influencing Acoustic Cavitation.....	25
2.2	Bubble Collapse Patterns	26
2.3	Material Response To Cavitation.....	29
2.4	Technical Surface Modification Technologies	31
2.4.1	Laser Shock Peening Technique	35
2.5	Cavitation Erosion Assessment Methods.....	54
2.5.1	Laboratory Techniques	54
2.5.2	Cavitation Erosion Progression.....	58
3	Experimental Design And Measurement	65
3.1	Experimental Goals.....	65
3.2	Experimental Setup Diagram	66
3.3	Procedure For Cavitation Erosion Test.....	67
3.4	Materials Description.....	69
4	Results.....	71
4.1	Sample Photographs.....	71
4.2	Cumulative Volume Loss And Volume Rate Loss	72
4.3	Surface Erosion Profiles.....	74
5	Analysis	76
5.1	Cumulative Volume Loss And Erosion Depth.....	76
5.2	Volume Loss And Erosion Depth Rates	78
5.3	Impact Of LSP Treatment On Cavitation Resistance	80
6	Conclusion	83
7	References.....	85
8	Appendix.....	97

NOMENCLATURE

Symbol	Description	Unit
R	Spherical bubble radius	[m]
R_C	Critical bubble radius,	[m]
R_o	Initial bubble radius,	[m]
R_L	Spherical liquid volume of radius	[m]
p_{in}	Vapor pressure inside the bubble	[Pa]
p_o	Ambient liquid pressure at the wall.	[Pa]
p_A	Peak negative acoustic pressure	[Pa]
p_B	Blake threshold pressure	[Pa]
p_g	Partial pressures of non-condensable gas	[Pa]
p_v	Partial pressures of vapor	[Pa]
t	Time	s
ρ_o	Equilibrium density of the liquid	[Kg/m ³]
μ	Liquid viscosity	[Pas]
A	Laser spot area	[m]
D	Unfocused beam diameter	[m]
DOF	Depth of focus	[m]
d	Spot diameter	[m]
E	Laser energy	[J]
F	Focal distance	[m]
f	Frequency	[s ⁻¹]
I	Laser intensity	[GW/cm ²]
P_{avg}	Average peak pressure	[Pa]
P_{peak}	Peak pressure	[Pa]
P_t	Pulse time	[ns]
Z	Reduced shock impedance	[Pas/m ³]
λ	Wavelength	[m]
M	Cumulative mass loss	[mg]
\dot{M}	Cumulative mass loss rate	[mg/min]
MDE	Mean depth erosion	[mm]
MDER	Mean depth erosion rate	[mm/min]

LIST OF FIGURES

Figure 1-1. Phase Diagram Depicting Boiling and Cavitation.	12
Figure 1-2. Pump Cavitation (a), Closing of Bi-Leaflet Prosthetic Valve (b.) [12, 13].....	15
Figure 2-1. Bubble Evolution Under Ultrasonic Cavitation. [33].....	19
Figure 2-2. Depicting Various Bubble Collapse Patterns.	26
Figure 2-3. Spherical Bubble Collapse Near Solid Wall. [47].....	27
Figure 2-4. CBS Pattern from Radiating Surface of Sonotrode. [50]	29
Figure 2-5. Plastic Deformation and Mass Loss of Surface Under Cavitation Erosion. [56]	30
Figure 2-6. Scheme of Laser Shock Peening.	36
Figure 2-7. Depth of Residual Stress in 0.55% Carbon Steel by Multiple Impacts. [75].	41
Figure 2-8. Surface hardness for AISI 4140 and Corresponding Peak Pressure [74].	47
Figure 2-9. Effect of Number of Laser Shocks on Fatigue Life for Ti-6Al-4V Alloy [74].	49
Figure 2-10. Direct Method (a), Indirect Methods of Vibratory Cavitation Apparatus (b). [95].....	55
Figure 2-11. Test Section of Cavitation Liquid Jet Apparatus. [98]	57
Figure 2-12. Characteristic Curve or Erosion Rate Versus Exposure Time.	58
Figure 2-13. Depicting Theoretical Cavitation Pit.....	60
Figure 3-1. Illustration of Experimental Setup for Cavitation Erosion Test.....	66
Figure 3-2. Components and Principle of Operation of UVCS.	67
Figure 3-3. Dimensions of the test sample for erosion test.....	69
Figure 4-1. Photographs of samples of cavitation erosion (a) reference (b) S/3/3 and (c) S/6/3	71
Figure 4-2. <i>Volume loss and rates as a function of exposure time, (a) reference and (b) S/3/3</i>	72
Figure 4-3. <i>Volume loss and rates as a function of exposure time, (c) S/6/3 and (d) all samples</i>	73
Figure 4-4. Surface profile evolution of eroded depth of samples.....	74
Figure 4-5. Mean eroded depth from single line measurement of profilometer.....	75
Figure 5-1. Comparison of volume loss and mean erosion depth as a function of exposure time.....	77
Figure 5-2. Comparison of volume loss and erosion depth rates as a function of exposure time.....	78
Figure 5-3. Comparison between mean depth erosion and compressive residual stress.....	80
Figure 5-4. Cavitation erosion resistance and incubation period of samples.....	81
Figure 5-5. Correlation between the erosion rate and the consumed time.....	82

LIST OF TABLES

Table 2-1. Comment on LSP Treatments of Different Materials Obtained from Literature.....	51
Table 3-1. ASTM32 Recommended Standards for Cavitation Tests.....	68
Table 3-2. Chemical and Mechanical Properties and LSP Process Parameters of Samples	70
Table 5-1. Final and averaged values of volume loss rates and erosion depth rates of test samples.	79
Table 8-1. Volume loss and mean depth erosion data for reference sample	97
Table 8-2. Volume loss and mean depth erosion data for S/3/3 sample	98
Table 8-3. Volume loss and mean depth erosion data for S/6/3 sample	99

1 INTRODUCTION

Cavitation describes the complex phenomenon of rapid formation and collapse of bubbles in a liquid when subjected to large pressure variations over time and distance [1]. When liquid pressure is reduced to sufficient low critical value, voids filled with dissolved gasses as well as the vapor from the liquid are created in the liquid. The implosion of the formed bubble occurs under violent compression which gives rise to intense micro streams that affect the material condition [2]. The formation of cavities and the dynamics of the bubbles are influenced by conditions including the quality of the liquid, wall geometry and roughness, nature, and state of flow as well as large pressure fluctuations, shock, and the vibration of the wall. Cavitation in liquids develops either as a result of great stretching forces or dissipation of supplied energy. In hydrodynamics, local constriction of channels resulting in accelerated flow with a significant drop in static pressure causes cavitation, due expansion of the liquid medium. In processes involving the use of laser streams, cavitation occurs as a result of dissipated energy during phase change gained from the local increase in the internal energy of the liquid [3]. Electrical and radiation-induced cavitation exists in addition to physio-chemical induced cavitation [4].

Significant effects of cavitation are observed in several applications. It is highly encountered in areas associated with the flow of liquids through channels with variable geometries. In hydraulic machinery, cavitation is noted for its detrimental effects on the performance and life degradation in machines such as pumps, turbines, propellers as well as biological prosthetics like artificial hearts [5]. Despite these effects, great potential has been drawn for various applications such as in environmental protection for the degradation of pathogens and it serves as a sound source in echo ranging survey in the ocean. Cavitation bubbles have also shown remarkable uses in the field of medicine for gene manipulation as well as for non-invasive methods of treating cancer [6].

Several techniques were developed to address mainly the detrimental effects of cavitation, especially in hydrodynamics. Amongst these were surface improvement which involves surface treatment s methods such as coating of metals surface with resistant alloys or materials and surface modification techniques which employs heat, chemical or mechanical treatment of the material surface to cause alterations with the material surface structure which improves the material resistance to damage [7]. Among these surface modification techniques includes the Laser Shock

Peening method. This method is used mainly to improve material hardness, strength as well as finishing by impacting a material surface with laser pulses which induce compressive residual stresses within the material. The depth of its effects is usually dependent on several process parameters of the laser and material [8]. Laser shock peening method has employed successively in various applications such as forming, shaping and coating inspection due to the effectiveness of desired properties namely, improved hardness, strength, and resistance to crack and corrosion with improved fatigue life in the hydraulic and medical device [9]. The purpose of this work mainly focuses on laser-treated material and response to the cavitation field.

This chapter presents the general idea surrounding the occurrence of cavitation including stages of cavitation bubble development and fundamental terms used in the description in *section 1.1*. Various classification of cavitation processes by the nature of the fluid, method of formation, bubble contents, and activity is also presented in *section 1.2* of this chapter along with the adverse and beneficial effects of cavitation in field applications in *section 1.3* and *section 1.4*

1.1 DESCRIPTION OF CAVITATION

Cavitation is defined as the rapid rupture of a volume of liquid that results in the formation of vapor cavities under very low pressures. Generally, any liquid contains voids known as ‘cavitation nuclei’, filled with gases and these voids exist at any time suspended in the liquid as well as on the liquid-solid boundary [10]. These voids are weak points within an initially homogenous liquid and are highly essential to the formation of cavitation under non-static conditions [11]. The onset of cavitation bubbles also called cavitation inception/nucleation, occurs when the static pressure of the liquid drops below the vapor pressure at the given temperature above the boiling point which induces the vaporization of the liquid volume for static conditions. Growth and rupture of bubbles as a result of nuclei formed due to intermolecular activity is termed as homogenous nucleation while heterogeneous nucleation is associated with rupture of voids that occur either between liquid and solid wall or liquid and suspended particles in the liquid [12]. Cavitation inception is a much similar case of phase change as boiling, driven by pressure gradients, and occurring at rapid rates since pressure changes in liquids are faster compared to temperature changes [3]. Phase diagram of the liquid substance as shown in *Figure 1-1*, is best used to distinguish cavitation

inception and boiling. The structure of liquid interface plays an important role in evaluating properties such as surface tensions and absorptions. An ideal liquid has no free interface and hence the appearance of vapor and gas bubbles accompanied with large tensile stress results when the pressure drops to a certain value. Ordinary boiling would occur with a sufficient drop in pressure [13]. The presence of free interface in real liquids with bubbles prevents large tensile stresses which allows rupture of vapor or gas bubbles following spontaneous formation and growth under rapid pressure drop.

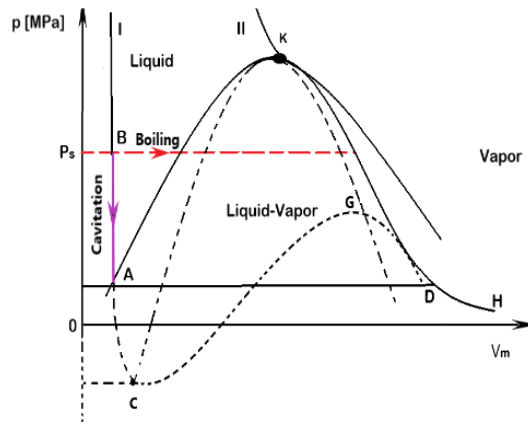


Figure 1-1. Phase Diagram Depicting Boiling and Cavitation.

From *Figure 1-1* above, saturated vapor pressure is represented by the equilibrium curve **AKH** which houses the metastable states with curve **CKD**. The development of vapor bubbles in a homogeneous liquid occurs on **AK** whilst the formation of liquid drops in the liquid is shown by **KH**. Ordinary boiling occurs along the isobaric lines, **Ps** with increasing temperature above saturation. When liquid pressure is dropped below **Ps**, on the same isotherm **I**, cavitation occurs. The process of cavitation governs three stages; nucleation, growth, and collapse of a single bubble or bubble clouds. Nucleation is the formation of bubbles within the fluid medium. Nucleation usually occurs in a narrow section of flow. This has been observed to occur in regions of reduced tensile strength within the liquid and liquid-solid surface. These sites are active gas microbubbles existing within the fluid and gas entrapped in crevices of particulates solutes. Under high-pressure drop, the bubble grows to maximum size, known as the resonant size where it oscillates around this size. In acoustic fields, a minimum constant negative pressure is required to cause and maintain

growth. Bubble collapse follows this stage after a sudden increase in pressure or during the compression cycle of the acoustic pressure wave. Collapse can be gentle or violent depending on the stability of the bubble during growth. The collapse of bubbles is characterized by two major forces; microjets and shockwaves. Microjets are produced when bubbles collapse asymmetrically as a result of wall interaction and shockwaves are produced during the symmetric collapse. In chemical reactions, bubble collapse is accompanied by light emissions [14].

1.2 CLASSIFICATION OF CAVITATION

Cavitation can be distinguished based on tensions existing within the liquid. When pressure pulse is induced in a liquid, the impact causes dispersion as a result of the vibration of the molecules [15]. The region of waves with low-density causes the onset of cavitation by the expansion of the liquid while the regions of high-density acts of compressive forces resulting in rupture of the formed bubble. The application of pulse can also cause the growth and rupture of preexisting microbubbles [16]. Cavitation occurring in this fashion is termed as *acoustic cavitation*. Rapid expansion and compression of fluid can also be observed in liquids flowing through constricted channels such that flow acceleration through the narrow passage can result in sufficient pressure reduction below the vapor pressure of the liquid. Vapor and gas bubbles formed causes cavitation to occur. This type of cavitation is known as *hydrodynamic cavitation* [17]. Cavitation can also be classified by local deposition of energy on elementary volumes of the liquid which creates local pressures with an increase in local internal energy to a value such that dissolved gases are released through a phase change. This process of cavitation controls the size of bubbles formed as well as their location with the liquid medium. If the rupture of liquid occurs as a result of high-intensity light or laser beam, it is termed as *optic cavitation*. And it's known as *particle cavitation* when elementary particles are used to cause rupture of the liquid medium [1].

Distinctive features are observed from the growth of vapor cavities in hydrodynamic cavitation which transforms the initially basic state of non-cavitating flow. Patterns formed by the cavitation bubbles can be grouped in two (2) stages from inception to the advanced form. The incipient stage is defined by the formation of microbubbles in a fully wetted flow influenced by reference pressure and flow velocity. Beyond the inception are three (3) types of advanced stages. Bubble growth

takes place next appearing as isolated bubbles moving along a solid body at low-pressure points or vortex or in high shear regions of blades and foils. This stage is known as *traveling cavitation*. The isolated bubbles tend to merge as a dense single vapor-filled sheet moving along the edges of blades and foil as they expand, shrink and collapse. Since cavitation contributes to the proliferation of nuclei in closed-loop, water tunnels are usually designed to provide sufficient time for gasses to dissolve [18]. Another advanced form is *fixed cavitation*. This situation occurs when liquid flow near the solid boundary detaches itself from the rigid flow passage such that cavities attach to the surface. It is usually experienced in constricted flows in orifice where lead velocity is increased at the loss of pressure head. Expansion of flow causes the fluid to separate from solid boundary accompanied by large frictional and pressure losses and eddies. As flow accelerates across the orifice, at a specific velocity, the pressure would fall below the vapor pressure resulting in cavities. Fixed cavitation is of two regimes: *sheet cavitation* found on the leading edge of the propeller blade and *attached cavitation* which is self-sustaining without a nuclei [19].

The third advanced form existing either in the fixed or traveling stage and is relatively structured is called *vortex Cavitation*. Cavities formed have their inception within a vortex core having a very low pressure compared to surrounding flow. Cases such as swirling flow in the draft tube or propeller tip of ships or pumps experience this cavitating flow [12]. When it appears in vortex core flowing from the load-bearing surface it is known as *tip cavitation* and *hub cavitation* when the vortex is spiraling away from load [17].

Bubble growth can be achieved by using dynamic or static means to reduce ambient pressure. The content of the bubble formed may determine the source of expansion [18]. Hence cavitation can also be classified on the contents of the bubble. *Vaporous cavitation* involves the growth of vapor-filled bubbles by the reduction in local static pressure below saturated vapor pressure at constant temperature followed by the implosion of the bubble due to a rapid rise in the local static pressure above the saturated vapor pressure. Implosion occurs at sonic speeds and very high temperature and pressure with light emissions, discharge of noise, shockwaves as well as microjets [19]. Vaporous cavitation is encountered in hydraulic machinery because of high erosion effects. When the bubble contains non-condensable gas, *gaseous cavitation* occurs, fueled by diffusion or pressure reduction and temperature rise. Growth and collapse of the bubble in this process result

in high noise and degradation of the liquid composition through oxidation. It is called *degassing* when the bubble is formed by diffusion [20].

1.3 ADVERSE EFFECTS OF CAVITATION IN FIELD APPLICATIONS

Cavitation is known to produce detrimental consequences in the hydrodynamic system as a result of impact loads exerted on material surfaces. The effects range from a reduction in performance and efficiency in propulsion and pumping systems to embolism, rupture, and bleeding vessels in biological systems [4]. In pumps, especially centrifugal pumps where suction eye end of design is significantly larger than the entry of the flow area, flow accelerates from suction through narrow flow area such that as pump flow rate increases, there is a significant drop in local pressure below vapor pressure to a value where bubbles are formed [21]. Bubbles are swept by impeller vanes to the trailing edge where the local pressure is greater than vapor pressure and bubble collapses. Bubbles collapsing closer to impeller blades release microjets at high velocities that cause pump degradation by creating pits on metal surface viewed as sponge-like structure (*Figure 1-2a*). A similar occurrence is observed in turbines creating unstable radial hydraulic radial forces resulting in fluctuations in flow rate and discharge pressure. The efficiency and performance of systems are decreased alongside with generation of noise and excessive vibrations that damage generator bearings and seals. Cavitation destruction mainly leads to fatigue and breakdown of material and system [22].



Figure 1-2. Pump Cavitation (a), Closing of Bi-Leaflet Prosthetic Valve (b.) [12, 13]

In biomedical applications, the impact of cavitation is heavily studied since negative effects may result in chronic diseases and possibly the death of an individual. The mechanism of the operation of artificial heart valves induces cavitation. In bi-leaflet valve design, cavitation occurs during the period before the closure of the valve where a narrow cross-section (*Figure 1-2b*), is created such that flow deceleration occurs with low pressures creating vortices and jet which causes rupture of blood cells and formation of clots in the blood stream[24]. The occurrence of cavitation is also observed in artificial hearts acting as pump and in head injuries and wounds where external impact force causes cavitation of cerebral fluid such that bubble collapse results in secondary injuries. In some biomedical applications of cavitation for beneficial purposes such as ultrasound cavitation where high intensity focused ultrasound (HIFU) is used in kidney, liver and tumor treatment, adverse effects such as lesions, ectopic embolism, vessel, and tumor rupture occurs. Cavitation causes the rupture of vessels around the tumor site which peels cancerous cells into blood circulation leading to embolism or cause cell injuries during lithotripsy in fragmentation of kidney stones [24,25].

1.4 BENEFICIAL EFFECTS OF CAVITATION IN FIELD APPLICATIONS

Despite the undesirable effects of cavitation in some systems, the principle of *supercavitation* where cavitation is employed in submarine technologies to increase speeds over several miles per hour. Speed in underwater is reduced due to shear forces acting tangentially on the surface of the submerged body creating a friction drag force that resists the motion [26]. To increase the speed in submarines or torpedoes, the nose is designed as a flat disk or cone which initiates cavitation bubbles under high speeds that reduce friction drag by creating an envelope around the body preventing contact between the liquid and surface body. This method has proven efficient in increasing the speed although difficulties are faced with achieving high speeds enough create to maintain cavitation bubbles [27]. Impact loads exerted on machinery during bubble collapse were investigated using cavitation jets and found to be significant enough to cause plastic deformation by inducing compressive residual stresses which prevents dislocation movements and thereby increasing the fatigue life of metals. This observation is employed as a surface modification technique known as *cavitation shotless peening* for improvement of fatigue life [28].

The use of ultrasound cavitation is rapidly growing wide in many biomedical applications. In diagnostic applications, cavitation gas bubbles of about 3 μ m encapsulated by protein, lipid or polymer shell, used as microbubble agents are injected intravenously to organ and tissue sites and excited by ultrasound to create contrast between tissues for contrast-specific, molecular and quantitative imaging. The use of microbubble agents is also applied in therapeutic purposes for drug delivery as well as gas and stem cell delivery to tissues and cell heating accompanied by ultrasound reactions is harnessed in fat emulsification and for treatment in weight loss [29] [30]. Other benefits of ultrasound cavitation are seen in cleansing applications. Ultrafiltration methods used in biochemical, dairy, and pharmaceutical industries result in the fouling of membranes from trapped proteins in pores. Mechanical agitation produced from oscillating bubbles are employed in cleaning. This effect is also used in water purification to destroy pathogens such as *Cryptosporidium* oocysts that are resistant to chlorine treatment while the production of peroxide and hydrogen gas is obtained from the recombination of free radicals from high temperatures released during bubble collapse [14].

2 CURRENT STATE OF KNOWLEDGE

This chapter introduces the present background knowledge involved in the initiation of cavitation with a focus on acoustic cavitation as well as current material modification solution techniques to cavitation problems mainly experienced by materials used in hydraulic systems. *Section 2.1 acoustic cavitation*, describes the fundamentals involving acoustic pressure amplitudes and energy involved in inducing cavitation, the nature of bubble evolution, stability, and collapse with varied pressures waves. Equations describing bubble stability and behavior in compressible and incompressible fluid and factors influencing the nature of acoustic cavitation is also presented in this section. *Section 2.2 bubble collapse patterns*, present bubble evolution patterns under different acoustic pressures. The process of bubble collapse and the effects of close bodies on the nature of collapse is described. *Section 2.3 material response cavitation* describes the basic interactions between cavitation and material surfaces leading to material degradation and failure in systems. *Section 2.4 technical surface modification technology* presents a general outlook on various material modification techniques and how they influence the properties of materials to be employed in cavitation damage solutions. The focus is placed on laser shock peening techniques in *subsection 2.4.1*, which is the current method being investigated in controlling the magnitude of cavitation damage. This method is used in treating the material for investigation under this current work.

2.1 ACOUSTIC CAVITATION

Acoustic cavitation occurs when the growth of bubbles due to a decrease in pressure and their subsequent rupture is affected by the propagation of an intense acoustic/ ultrasound wave [16]. Bubbles generated here are called *acoustic bubbles*. The presence of alternating pressure field is necessary for acoustic cavitation to occur otherwise bubbles undergo dissolution. Low radiation intensities cause preexisting bubbles to grow larger [31]. This increases the surface area of bubbles for the diffusion of dissolved gas into the bubble under low pressure until bubbles reach a peak size known as *resonant size* where they oscillate around this size. The rapid expansion of bubbles

usually occurs under the negative half cycle of high acoustic pressures such that a violent collapse occurs in the compression cycle into smaller bubbles [32], as shown in *Figure 2-1* below.

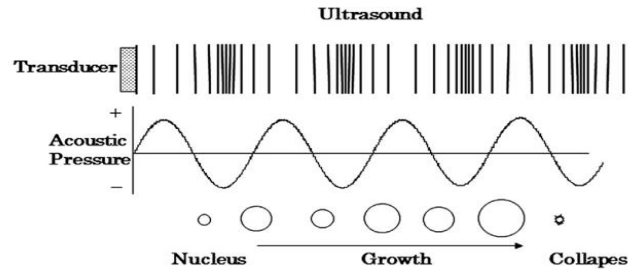


Figure 2-1. Bubble Evolution Under Ultrasonic Cavitation. [33]

According to the hot spot theory, the collapse of the bubbles is adiabatic which results in extreme temperatures and pressures in small transient regions of the liquid [34]. Shockwaves, noise as well as liquid jets are generated from the extreme temperature and pressure. When light emissions are involved in bubble collapse, it is termed *Sonoluminescence*. High-power *ultrasound* of frequency ranging from 20 kHz to several MHz is mostly employed to induce acoustic cavitation [35].

Cavitation bubbles do not generate the same effect especially for beneficial purposes such as ultrasonic cleaning. The amount of energy introduced to the bubble as well as the ambient condition and nature of the liquid around the bubble distinguishes the mechanism of collapse as *stable* or *transient* [36]. Bubble size depends on the amount of energy, the nature of the liquid and ambient conditions determines the degree of dissolved gases and the rate of vaporization. The varying acoustic wave produces a mechanism of collapse that is either gentle or violent. Stable cavitation is distinguished by a limiting radius value where bubbles oscillate around some equilibrium size for many cycles of acoustic pressure and may sometimes be permanent. Based on the lifetime of the bubble, a stable cavitation bubble leaves a “*seeding*” bubble that oscillates steadily for successive growth after the collapse. The *seed bubble*, if buoyant may float on the liquid surface [37]. This happens during degassing.

Oscillation of stable bubbles is visibly observed in cavitating fields to occur over long-time scales with heat and mass transfers producing considerable effects as seen in microstreaming. When the

acoustic amplitude at which the stable bubble is oscillating is increased to a threshold pressure value, P , mass diffusion occurs which results in the growth of bubble proportional to increase in pressure such that the bubble would eventually develop into a transient bubble and collapse. In transient cavitation, bubble growth occurs rapidly in less than one cycle often expanding to twice the original size. Small bubbles produced on violent collapse after a few acoustic cycles and dissolves into the liquid or merge to form a larger active bubble. If a small bubble is sufficient in size, it can be active by itself. The magnitude of violent collapse is dependent on the bubble content. Since it occurs in short times, it is assumed that mass diffusion is significantly limited although condensation and evaporation occur constantly. For a gaseous bubble content, due to low molecular weight as compared to vapor, mass transfer is insignificant and bubble maintains a constant gas content producing less violent collapse. Vaporous bubble however at a given temperature have higher pressures at saturation, vary in mass, and produces more violent collapse [38]. Transient cavitation produces high-pressure shock waves that lead to erosion and used in ultrasonic cleaning. Considering the activity of the bubble collapse, stable cavitation is considered inactive whilst transient is active due to light emission on the Raleigh collapse[39].

2.1.1 ACOUSTIC BUBBLE DYNAMICS

In acoustic cavitation, the local pressure drop in the liquid is required to be decreased to a negative pressure for bubbles to be generated because pressure below saturated vapor pressure has been observed as not sufficient to induced bubble growth. This negative pressure is needed in the rarefaction cycle to breakdown the cohesive forces of the liquid. Wavelength is inversely proportional to frequency. As the frequency of the ultrasound increases, wavelength decreases hence reduced rarefaction and compression phase. This results in difficulty in creating bubbles hence minimum conditions for pressure-amplitude of the wave must be set to sustain rarefaction and compression phase. The minimum pressure amplitude required for acoustic cavitation to occur is called the *Cavitation threshold*. Two different pressure amplitudes; nucleation and collapse threshold are significant to sustain the steady growth of the bubble as well as the collapse. Extreme negative pressures are usually required in degassed liquids for nucleation to occur An example by

Yasui [33] on water also showed that the degree of dissolved gas in a liquid plays a significant role in determining the threshold of cavitation.

Several studies are being conducted to explain the occurrence of cavitation erosion by analyzing the bubble pulsation and collapse along with heat and mass transfers during the process. Certain investigations obtained a relation such that the cavitation pressures are one-fifth of the liquid viscosity whereas damping effects arising from liquid viscosity were considered and non-dimensional numbers introduced such that collapse of the bubble is slowed down [11]. To understand the dynamics of bubbles, pressure and velocity fields are evaluated using laws of conservation of mass, energy, and momentum to obtain a value for velocity and pressure at any point where the bubble oscillates is influenced by a time-dependent pressure. Solutions to bubble dynamics are distinguished based on stable states and the motion of bubbles under a critical growth radius. Blake cavitation threshold defines stable and unstable states by a critical radius in equilibrium at which an arbitrary bubble within the liquid would either expand without bounds or contract and dissolve into the liquid. As pressure dominates the dynamics of the bubble, a threshold pressure known as the Blake threshold pressure is introduced as the static acoustic pressure beyond which bubbles subjected would experience quasistatic expansion without bounds. The evolution of bubbles with radii slightly under the critical radius value occurs with rapid changes in short durations is described by the Rayleigh – Plesset equation [40].

Blake's threshold cavitation model considers the case of a spherical bubble filled with vapor and non-condensable gas. The existence of surface tension ensures that the pressure within the bubble is higher than the liquid pressure at the wall. The surface energy per unit area is termed *surface tension* (σ). For a spherical bubble of radius, R and surface energy is $4\pi\sigma R^2$, the work needed to expand the bubble in radius by dR is $8\pi\sigma R dR$ obtained by an increase in surface area and neglecting the term dR^2 in relation below [20].

$$4\pi\sigma(R + dR)^2 = 4\pi\sigma R^2 + 8\pi\sigma R dR \quad (2.1)$$

The force used in expansion bubble is given by the work per unit distance moved, dR . Given the physical fact that the bubble never achieves equilibrium, a force balance between the inside and outside the bubble is assumed in analysis neglecting vapor to achieve pressure relation;

$$p_{in} = p_o + \frac{2\sigma}{R} \quad (2.2)$$

Where p_{in} represent the gas pressure inside the bubble and p_o is the ambient liquid pressure at the wall. The term $(2\sigma/R)$, is known as the *Laplace pressure*. It is a function of the wall radius that depicts how greater the inside bubble pressure is to the liquid pressure at the bubble wall. This equation can be rearranged to introduce a value of the radius, the critical radius, R_c for stability as;

$$R_c = \frac{2\sigma}{(p_{in} - p_o)} \quad (2.3)$$

Such that an unstable condition is defined if the radius $R < R_c$, the bubble contracts where the surface tension is predominant and if $R > R_c$ the gas pressure dominates and the bubble expands. Following this, it can be said that at equilibrium pressure inside a bubble must be $(p_o + 2\sigma/R_o)$ at an initial time, $t=0$ and initial radius, R_o . In acoustic cavitation, bubble growth occurs from the application of ultrasound which resets the equilibrium condition when a minimum pressure amplitude p_A is applied at the time, $t > 0$ for a steady bubble of radius R_B greater than R_c to grow to a Blake threshold. Thus, the following relation holds for the new equilibrium condition;

$$\left(p_o + \frac{2\sigma}{R_B}\right) \left(\frac{R_B}{R}\right)^3 = p_o - p_A + \frac{2\sigma}{R} \quad (2.4)$$

The gas pressure due to isothermal expansion is represented by the left term while p_A represent the peak negative acoustic pressure. This relation gives meaning to the quasistatic changes in liquid depicting a uniform but slow changes in liquid pressure during bubble evolution without the effects

of fluid inertia and viscosity. From this relation, by expressing $\partial(p_o - p_A)/\partial R$, Blake threshold pressure, p_B can be obtained as *equation (2.5)* where the critical radius is given by *equation (3.6)*;

$$P_B = P_O + \frac{8\sigma}{9} \left[\frac{3\sigma}{2(P_O + 2\sigma/R_B)R_B^3} \right]^{1/2} \quad (2.5)$$

$$R_{crit} = \left[\frac{3R_B^3(P_O + 2\sigma/R_B)}{2\sigma} \right]^{1/2} \quad (2.6)$$

Considering bubbles with a subcritical radius the violent collapse of the bubble can be described by the Rayleigh-Plesset equation which governs the growth of bubble radius under the effects of time-dependent pressure fields in an infinite incompressible fluid. Derivation by Yasui [20], considers a spherical liquid volume of radius R_L surrounding a spherical bubble of radius R with center at of spherical bubble. For the spherical shell of radius r and thickness dr , the kinetic energy of the liquid volume may be expressed as the product of its mass and velocity as;

$$dE_k = \frac{1}{2} (4\pi\rho_o r^2 dr) * \left(\frac{dr}{dt} \right)^2 \quad (2.7)$$

Where ρ_o is the equilibrium density of the liquid and integration of this concerning radius r from R to R_L .

$$E_k = \frac{1}{2} \rho_o \int_R^{R_L} \left(\frac{dr}{dt} \right)^2 4\pi r^2 dr = 2\pi\rho_o R^3 \left(\frac{dR}{dt} \right)^2 \quad (2.8)$$

When bubble expands, the liquid volume also expands and work is done on surrounding liquid, while on bubble collapse, liquid volume contracts and work is done on the bubble by the surrounding liquid. Thus, the negative work done exerted on the surrounding liquid by both bubble and liquid volume can be expressed as;

$$W_{bubble} = \int_{R_0}^R 4\pi r^2 p_o dr \quad (2.9)$$

$$W_{liquid} = p_\infty \Delta V = p_\infty \int_{R_0}^R 4\pi r^2 dr \quad (2.10)$$

Where R_0 is the instantaneous bubble radius, p_∞ is the sum of ambient liquid pressure plus instantaneous acoustic pressure exerted on the surface of the liquid volume. Differentiating *equation (2.8), (2.9) and (2.10)* and applying the law of energy conservation below yields a bubble boundary $R(t)$ relation in *equation (2.11)*.

$$\frac{\partial(W_{bubble})}{\partial R} = \frac{\partial E_k}{\partial R} + \frac{\partial(W_{liquid})}{\partial R} \quad (2.11)$$

$$\frac{p_o - p_\infty}{\rho_o} = \frac{3}{2}(\ddot{R}^2) + R\ddot{R} \quad (2.12)$$

Where \dot{R} and \ddot{R} are the first and second derivatives of the radius with time, t. and the term $[p_o - p_\infty]$ is the pressure difference that influences the evolution of the bubbles under acoustic pressure application. When the bubble wall is in motion, the effects of viscosity on the bubble boundary is factored in *equation (2.12)* to obtain;

$$p_o = p_g + p_v - \frac{2\sigma}{3} - \frac{4\mu\dot{R}}{R} \quad (2.13)$$

Where p_g and p_v represent the partial pressures of non-condensable gas and vapor and μ is the liquid viscosity. Following this, the Rayleigh-Plesset equation is derived by inserting *equation (2.13)* into *equation (2.12)*.

$$R\ddot{R} + \frac{3}{2}\dot{R}^2 = \frac{1}{\rho_0} \left[p_g + p_v - \frac{2\sigma}{R} - \frac{4\mu\dot{R}}{R} - p_s - p_A(t) \right] \quad (2.14)$$

p_s represents the ambient static pressure, $p_A(t)$ is the instantaneous acoustic pressure at a time t . This equation presents a solution to the evolution of a bubble in an incompressible fluid but is not valid upon the violent collapse of the bubble at the speed of sound [41].

2.1.2 FACTORS INFLUENCING ACOUSTIC CAVITATION

In laboratory experiments, cavitation is induced using acoustic fields to study characteristics surrounding field operations, and thus, it is of importance to optimize factors influencing cavitation thresholds such as minimum pressure amplitude required to initiate growth and collapse of the bubble. Cavitation threshold and intensities depend on fluid properties and acoustic wave properties such as frequencies, viscosity, intensity, and amplitudes of the wave as well as external fluid pressure. Cavitation intensity decreases with increasing acoustic frequency. Therefore, longer periods are required for bubbles to reach maximum bubble size, sufficient to cavitate. At increased frequencies, duration of rarefaction cycle is reduced such that bubbles do not achieve resonant frequency and consequently less cavitation intensity. In effect, large intensities are required to facilitate bubble growth and cause unstable bubbles to undergo Rayleigh collapse.

Maximum bubble size and quantity increases with large pressure amplitudes resulting from an increase in acoustic intensity. However, Rayleigh's collapse time increases with increasing maximum bubble radius such that if collapse time exceeds the duration of the compression cycle, a lower number of bubbles would collapse. Owing to this increase acoustic intensities are optimized with Rayleigh collapse time equal or less than the duration of the compression cycle. Violent bubble collapse at larger pressures is observed with an increase in intensity as a result of increased ambient pressure. Other factors such as liquid temperature influences the cavitation threshold. At reduced temperatures, viscosity and surface tension becomes dominant such that cavitation threshold is increased and bubble collapse yields lower pressures and temperature for high-temperature fluid medium [9, 17, 18]

2.2 BUBBLE COLLAPSE PATTERNS

The prospects of diminishing the effects of cavitation damage especially in hydrodynamics lead to several studies on cavitating bubble characteristics including bubble evolution and collapse patterns. The nature of the oscillating bubble collapse pattern relates to the magnitude of damage on materials. Acoustic pressures do not affect isolated spherical bubbles of a very small radius than resonance radius and hence these bubbles do not oscillate [31]. If the bubble contains a gas of uniform and constant density, the Laplace pressure has no effect and mass transfer is controlled by *Fickian diffusion* such that the bubble can be observed to shrink by the diffusion rate, a process known as dissolution (*Figure 2-2a*). A similar occurrence is observed when liquid is under decompression or heating which causes the growth of the bubble (*Figure 2-2b*). A bubble oscillating under its natural frequency below the resonant bubble size would undergo low amplitude oscillations (*Figure 2-2c*) when driven by different pressure frequency such that the energy is dissipated through thermal and viscous damping. The amplitude of this type of oscillation decays for a short pulse (*Figure 2-2d*) unlike the application of a continuous wave. Under high acoustic pressures, the bubble undergoes sudden rapid expansion and collapse to release fragments (*Figure 2-2e*) or possibly undergo the growth and collapse over several cycles. Bubble pattern depicted in *Figure 2-2f* would occur if the bubble under high-pressure amplitude is closer to a resonant size such that surface waves; shimmer is observed on bubble surface with break off of microbubbles from the tips. The spherical shape of the bubble is dominated by surface tension hence bubbles lose sphericity with an increase in radius. Due to this occurrence, bubbles exhibit different collapse patterns around structures such as a rigid wall, air bubbles, and may even depict bubble structure owing to the radiation surface of transducers [43].

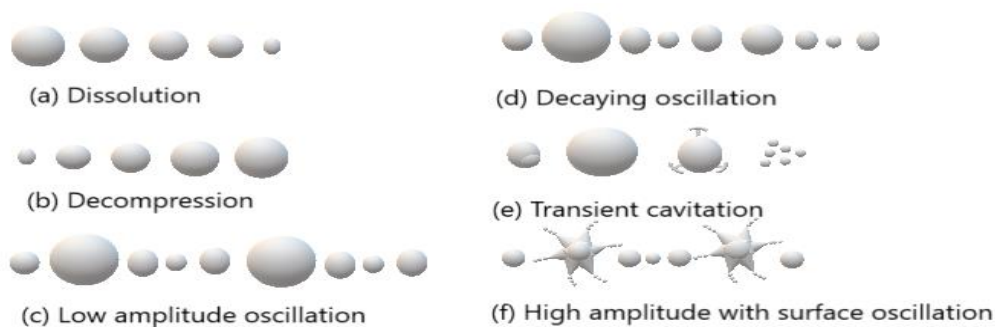


Figure 2-2. Depicting Various Bubble Collapse Patterns.

Three main activities leading to cavitation damage are the effect of microjets when bubble collapse towards a rigid wall, the splashing effect upon contact as well as shockwave reaching amplitudes sufficient to cause material deformation [44]. During the collapse, the volume of the bubble decreases with an increasing velocity at the center towards the wall. Large external pressure differences are generated on bubbles close to wall vicinity due to high velocities. In this situation, the Laplace pressure is insufficient to support the bubble structure such that the upper surface caves into the bubble causing a microjet to form perforating the other side of bubble towards the wall at velocities high enough to induce plastic deformation on the wall with the process depicted in *Figure 2-3* [45]. Following the effect of microjets, flow is observed to move radially which in turn results in secondary evaporation known as *splashing*. Several microbubbles are formed generating shockwaves on the material surface. The formation of microjets in the acoustic field is observed to occur only when velocities of the bubble collapse higher than the velocity of the propagating wave [46].

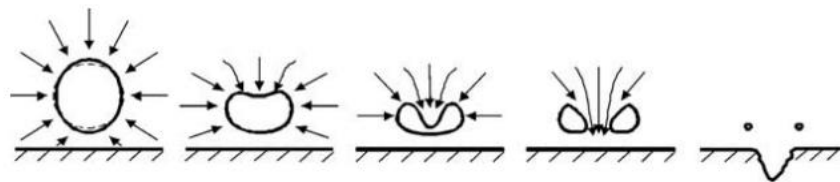


Figure 2-3. Spherical Bubble Collapse Near Solid Wall. [47]

Investigations performed by Muller et al [48] to identify bubble collapse patterns close to a solid wall at a varied distance using both optical and acoustic methods confirms that the formation of microjets is influenced by close interactions of the bubble with the wall. For bubbles collapsing at a far distance from the wall, the magnitude of impact force diminishes successively from the first bubble collapse. They also discovered that bubbles collapsing near-wall without touching the wall during initial expansion was influenced by wall interactions resulting in microjet formation after the first collapse. Impact force nonetheless diminishes with subsequent collapses occurring directly at the wall. Unlike the previous collapses, the magnitude of impact force from the second bubble collapse is much higher than the first bubble collapse occurring directly at the wall due to

a sucking effect created at the wall. Owing to these observations, an expression of bubble–wall dimensionless distance, γ ($\gamma = h/R_{max}$), where h is the distance from bubble center to wall and R_{max} is the maximum cavitation radius at collapse, was considered to play a major role to determine the event of cavitation damage at values of $\gamma \leq 2$ with microjets occurring at values of $\gamma \leq 0.7$. Studies of bubble collapse around structures such as air bubbles showed different characteristics. Jing et al [49] discovered the cavitation bubble in the presence of the air bubble would always collapse towards air bubbles while the final direction of collapse in the vicinity of the air bubble and wall is a resultant of the attractive and repulsive forces of both structures. They also observed cavitation bubbles penetrating very close air bubbles during expansion and stretching upon collapse and may even merge, for a shorter distance to form a gas cavitation bubble such that the magnitude of violent collapse is reduced. The effect of the air bubble on the wall is essential in reducing aeration and cavitation damage.

Further research of bubble structure in *sonochemical* experiments reveals a cone-like bubble structure (CBS), formed close to the radiating surface of the transducer which is presumed to influence the yield of chemical reactions. Moussatov et al [50] discovered that, in the vicinity of a cylindrical radiating surface of sonotrode immersed in the water tank, bubbles formed disengage from their stable region of radiating surface and hurdle to form streamers that align along the axis of the surface towards the base of the tank with an increase in intensity (*see Figure 2-4a*). They also realized that the formation of CBS is hindered by increase turbulent currents near the radiating surface as the diameter of sonotrode is reduced (*see Figure 2-4b*). CBS formation was explained as the effect of Bjerknes force defined as the average translation force applied on a pulsating bubble by a periodic sound pressure field [31]. High amplitudes create a high-pressure zone extending from the surface along the symmetric axis of sonotrode with decreasing intensity to a few centimeters away. Primary Bjerknes force reverses at high-pressure amplitude creating a repulsive zone around the symmetric axis such that bubbles drawing away from the surface are repelled into radial channels with zero Bjerknes force. The secondary Bjerknes force which exists between bubble controls the formation of a large streamer. The repulsive zone disappears at a larger distance away, hence drawing the bubble into attractive zone forming the apex of the inverted cone structure [51]. CBS generates high chemical activity observed in chemiluminescence (*see Figure 2-4c*).

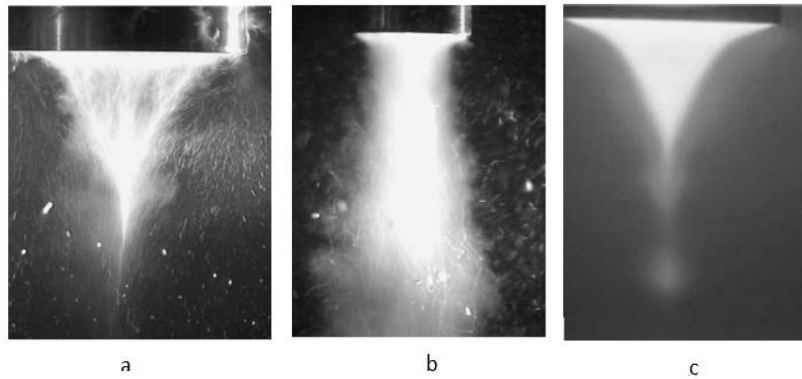


Figure 2-4. CBS Pattern from Radiating Surface of Sonotrode. [50]

2.3 MATERIAL RESPONSE TO CAVITATION

In the field applications, especially hydraulics, one of the most common concerns deals with material degradation. Due to loss of mass, surface deformation, structural vibrations as well as appearance altogether leading to fatigue and failure of components. As mentioned earlier, one of the results of rapid growth and collapse of cavitation bubbles is the release of microjets at extreme pressures capable of causing plastic deformation in materials. Due to difficulty in measuring pressures produced by bubbles, an estimate of the stress-impact pressure on solid bodies reported by *Momma et al* [52] from experiments ranges from 4.8 to 10 GPa. In reality, if stresses impacted on the solid surface are capable of removing the existing passive film and the rate of replacement by a corrosion product layer determines the rate of mechanism, it is termed as *cavitation erosion-corrosion* or *cavitation damage* [53]. The magnitude of cavitation damage on the material structure is determined by the degree of aggressiveness of the flow with a damaging cycle comparable to a fatigue cycle where a load of impact and its frequency influences the fatigue life. Low-cycle fatigue (LCF) is would be caused by larger amplitude impacts at low frequency. Under this mechanism, materials tend to have shorter lifetimes with large areas of plasticity. Longer lifetimes with small or negligible areas of plasticity relates to low-cycle fatigue (HCF) caused small-amplitude impacts at high frequency [54].

In a cavitation study by Fatyukhin et al [55] on metal samples, a relative increase in micro-hardness was observed with a decrease in sub-roughness. Stress-induced stresses by a single cavitation bubble contribute to strain deformation which increases the hardness within the surface on the material caused by impact stress exceeding the elastic limit. Mass loss and plastic deformation accompany ultrasonic cavitation erosion, which is best described by volume changes. According to *Fushi et al* [56], volume changes are proportional and have a positive relation with exposure times and increasing driving current. Despite this general embodiment of ultrasonic cavitation using volume changes, it is quite difficult knowing where the incubation time ends. It becomes imperative that; the incubation time is well defined and its relation to volume changes well established. The erosion process first begins with the incubation period followed by the cavitation erosion. High plastic deformation and low mass loss characterize the incubation period, meaning that the plastic deformation is the major parameter for the determination of the incubation period. From *Figure 2-5* below, the pits caused by multi impacts first eroded the oxide layer, a shot process with less plastic deformation, followed by grain refinement. This second stage has high plastic deformation which improves on hardness, increase in residual stresses as well as changes in surface properties. Consequently, hardness, residual stress as well as stress strain effect on materials is necessary to understand and predict the effect of cavitation on the fatigue life on components.

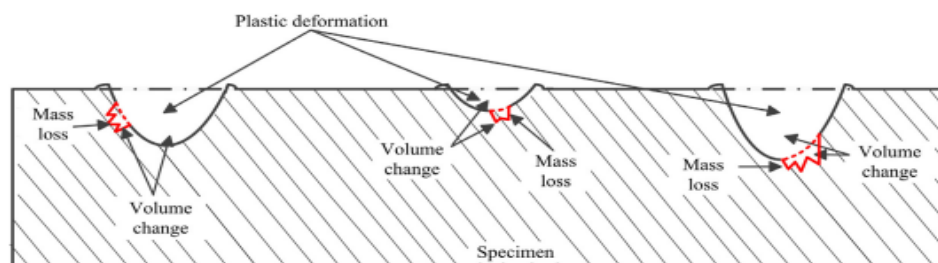


Figure 2-5. Plastic Deformation and Mass Loss of Surface Under Cavitation Erosion. [56]

2.4 TECHNICAL SURFACE MODIFICATION TECHNOLOGIES

Surface engineering is progressively important in present-day production processes and requires inherent state-of-art technologies purposed to improve material performance, appearance, and life. Designers are therefore challenged with establishing innovative surface treatment techniques interspersed with product specifications, production costs along with ecological aspects of material production. The material surface is the entryway to mechanical, thermal, chemical, and electrochemical interactions with the environment. These interactions translate to corrosion and wear resistance, tribological, optical, and decorative and matched interface behavior. The final part surface to be created depends entirely on the loading conditions the material would be subjected to and appropriate surface treatment would prevent or delay damages [57].

Loading conditions are of two main kinds; volume and surface loads. Cavitation damages are controlled by surface technology which addresses loads, stress, and their impact and material responses. Surface technology concentrates on producing part surfaces of material using protective coating or modifying the surface zone of the material [58]. There are several different types of coating and surface treatment methods used to improve qualities such as hardness and erosion resistance. The method of coating involves covering the surface of a workpiece with a well-bonded layer of shapeless material and the quality of the process is dependent on the bond strength between the coat and the surface. Unlike a coating, the surface modifying techniques involves the application of some energy form to alter the material surface to some depth. This study focuses on surface modifying technologies to improve cavitation erosion resistance.

As discussed earlier, erosion and corrosion mechanism arise mainly from surface loads. The impact of cyclic stress from cavitation bubbles results in fatigue, creep, pitting, and erosion of the material. Attempts to obtain material properties that can be improved to enhance cavitation resistance proved difficult, nonetheless, a relation of the cavitation dynamics to fatigue mechanism due to similarities in accumulation of impacts provided a direction of utilizing fatigue resistance factors and this concept has proved successful over the years [59]. Several factors including hardness, grain size, uniform microstructure, and compressive residual stresses (CRS) have been identified to improve cavitation resistance. CRS reduces material failure by inducing a plastic layer which external tensile stress must overcome to propagate the crack. Cracks do not initiate or grow in a plastically deformed layer hence most surface modifying techniques concentrate on improving

erosion resistant properties especially by inducing CRS due to lack of plasticity in failing materials. Modification techniques can be grouped into three (3) categories; thermal, thermochemical, and mechanical treatments [60].

In *thermochemical treatments*, a modified phase of the material structure is obtained by diffusing decomposed solid, liquid, or gas into the lattice of metals. Resulting properties are highly dependent on the decomposed substance, its reaction with the substrate material as well as the temperature involved in the process. When nitrogen is diffused into substrate material the process is called nitriding. The process involves dissociation and diffusion of ammonia at high temperatures on the substrate surface forming a nitride layer without a phase change of material [61]. Among the nitriding processes includes plasma nitriding, liquid-salt nitriding, laser nitriding, and gas nitriding. Liquid-salt nitriding is conducted in nitrogen-fused salt-baths such as NaCN and Na₂CO₃.

Some percentage of nitrogen and carbon is diffused into the surface of iron-based metals within a short cycle time but the process very toxic and produces low quality of nitride layer and therefore not commonly used. Plasma nitriding is an industrial metal treatment involving the ionization of the gas molecules in a chamber with the substrate material. The high voltage energy accelerates nitrogen gas molecules towards the material surface. Their impacts result in diffusion into the surface to form a nitride layer. Higher surface hardening can be achieved with this process but non-uniformity of higher temperatures may result in surface damage of material.

Similarly, in Gas nitriding (GN), there is dissociation and diffusion nitrogen to form hard nitride precipitations in the surface of the material in a vacuum. Li et al [62] investigated the effects of *gas nitrified* pure Ti and Ti-6Al-4V alloy on cavitation erosion and reported an increase in the number of cracks and pits at high nitriding temperatures of 1123 and 1273 K. Although an increase in micro-hardness and thickness of the nitrogen diffused zone occurred at high nitriding temperature, a greater weight loss was experienced within a short period of exposure to cavitation. Indicating that cavitation could easily destroy surface and resistance is not entirely dependent on surface hardness [63]. GN processes consume excessive energy in industrial applications due to long cycle duration at high temperatures and this results in low production efficiency. Pressurized gas nitriding (PGN) was introduced to improve efficiency. Wang et al [64] reported an increase in surface hardness as well as great wear resistance which was controlled by the nitriding pressure

using the PGN method. These thermochemical processes overall, aim to increase wear and fatigue resistance through surface hardening and are highly used for gears, shafts, and valves. Other thermochemical processes named after the solute particle used such as boronising, carbonization, carbonitriding, and aluminizing results in varying degrees of surface hardness improvement [61].

Another category of surface modification is by *thermal treatments*. Thermal treatment processes improve material surface without a change in chemical composition. Substrate materials are heated to high temperatures and cooled rapidly. Some major thermal processes are electron beam and laser treatment, flame or induction hardening, and ion implantation. The first two (2), similar in mechanism involves subjecting the material to a laser or electron beam of high density to cause changes to surface structure. Application of high temperature with rapid quenching in laser treatment creates fine grains boundary which resists dislocation motion, hence improving surface hardness. The treated layer has sufficient thickness, high hardness, and wear resistance with a change in material properties [65].

Flame and induction treatment uses the same principle of creating fine grain size, increasing erosion resistance at a greater depth of material surface by heating and quenching to prevent phase transformations. Ion beam implantation on the other hand uses plasma to impinge gas atoms into ions, and embedded into the material lattice to create atomic defects that improve hardness. Ion implantation used as an alloying method to improve cavitation erosion resistance was relatively high in nickel than copper and was observed to prolong the incubation period to erosion although Karimi [66] reported no significant effect on 1812 austenitic stainless steel under the same process.

Mechanical surface treatments involve elastic-plastic cold-working of a surface to enhance material properties. The process of inducing mechanical stresses instead of heat to permanently alter the crystalline structure to increase strength is termed *Cold working*. Defects are created in the crystalline structure of the material which reduces the motion of crystals and hence material becomes more resistant to deformation [67]. The surface layer is work-hardened by the process, generating residual stresses which improves performance under cyclic loading. This study focuses on non-cutting mechanical surface treatments. Processes such as deep rolling (DR), abrasive blasting, and laser shock peening (LSP) are non-cutting methods [60].

The deep rolling method is divided into two based on the symmetry of the material part. Symmetry in a deep rolling process is very significant to determine which of the two existing methods to be

used. A typical DR machine consists of three balls, spaced around a workpiece at 120°. The axially symmetric workpiece is deep rolled by moving the workpiece rotating on its longitudinal axis as well as displacing on the same axis against the three balls while the DR machine is not moving. For other symmetries and complex geometries, the pressure is applied by a mechanically or hydraulic controlled ball or roller moving on opposing sides against the surface of the workpiece. Deep rolling is entirely used to cause plastic deformation and induce CRS by a controlled ball or roller applying specific pressure to a smooth, slightly, or heavily notched workpiece. This process also reduces surface roughness and causes strain hardening [68]. It is generally performed on machine tools for geometric accuracy purposes and whiles increasing fatigue strength.

Abrasive blasting method uses coarse media particles concentrated at high speed on the material surface usually to smooth a rough surface, roughen a smooth surface, and shape a surface or to remove shot contaminants. Depending on the type of media used, this process can be divided into several variants with major kinds being sandblasting shot blasting and shot peening [60]. In *sandblasting*, the abrasive media use is sand mixed with air in a compressed chamber which is propelled under high pressure against the surface through a nozzle. Although the sand is readily available and most economical to use, it is rarely used due to respiratory health issues from inhaling silica particles. The method is generally used for smoothening, shaping, and cleaning metal surfaces.

Unlike sandblasting, *shot blasting* uses a spinning wheel to accelerate abrasives ranging from glass, plastics to metals against the denser metal surface for deeper penetration. Shot blasting is mainly used for removing a layer of the material surface as the cleaning process and serves as a preparation technique of material for coating and painting. Nonetheless, this method also promotes material strengthening against wear [69]. The shot peening method is like shot blasting but serves the purpose of reducing residual stresses in material from manufacturing processes. The process involves shooting rapid streams of spherical steel balls ‘shots’ to the material surface. The impact creates a dimple in the metal surface introducing compressive stresses into the metal as it expands under the force. This improves the endurance of the metal against wear and also improves fatigue strength [70].

2.4.1 LASER SHOCK PEENING TECHNIQUE

Laser shock peening (LSP) is a relatively new surface treatment technique, considered as an advanced substitute of the conventional shot peening with the ability to penetrate material surface at higher depth to induce residual stresses [71]. The flexibility of this technique popularizes it in several areas especially with metal parts of complex geometries which cannot be treated effectively with shot peening. LSP techniques are also employed in biomedical fields together with alloying produce better surface integrity and corrosive resistant implant to minimize the effect of stress shielding [8]. Dents formed during the process was found to aid in cell adhesion and growth on implant surface due to porous structure produced. The technique imposes large load cycles on materials by impacting high-pressure shockwave greater than the dynamic yield strength of material within microseconds to cause local plastic deformation and induce CRS [72]. In laser shock peening, a focused high-power laser is directed unto a material surface which sends a shock wave through the material. This shock wave due to momentum energy transfer, high compressions, and rarefactions creates residual compressive stresses from the plastically deformed surface to a depth in the material which is proportional to the power of the laser. There is an inverse relationship between the compressive stresses and the depth from the surface into the material. In the process of increasing the residual compressive stress, the number of dislocations also increases and thereby increasing the hardness of the material. The fatigue strength and fatigue life of the material increase with an increase in the hardness of the material. LSP is also used to produce a good surface finish of metals with refined microstructure [73].

2.4.1.1 Description of Laser Shock Peening Process

On contact with the surface of the material, the first thing formed by the high-intensity laser is plasma. To prevent the material from melting, it becomes necessary for the surface of the materials to be coated with absorbent material. A myriad of materials has been used as absorbent materials, with black paint being the most effective. The absorbent material does two things; preventing the melting of the material and laser ablation, to effectively transfer the pressure to a shock wave [74]. Also, a confining medium layer is needed to intensify the shock at a given area by preventing the

expansion of the plasma of the material surface. Also, research shows that the confining medium layer can increase the plasma pressures on the material surface from 5 – 10 GPa, thereby increasing the compressive stresses generated in the material [75]. This layer, called the tamping layer is usually thin and transparent. So many materials have been used as the tamping layer including water, quartz, and glass and the choice depends on parameters like the density of the tamping layer relative to the material substrate, the acoustic impedance effect, and other properties of the material substrate itself. *Figure 2-6* below illustrates the process of laser shock peening process.

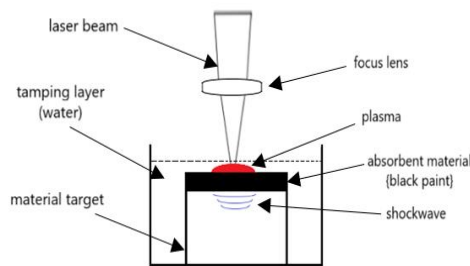


Figure 2-6. Scheme of Laser Shock Peening.

After the intensification of the laser concentration and confinement, the substrate material surface begins to plastically deform if the impact wave energy is greater than the dynamic yield strength of the material. The shock wave attenuates as it propagates with material depth while material deformation decreases after peak stress falls below the dynamic yield strength [76]. The deformation of the substrate material changes the microstructure of the material by greatly increasing the dislocations and the dislocation motions of the material presenting a state of CRS due to constraints imposed by surrounding regions of material. Due to this, certain properties of the material like hardness, wear, fatigue limit, and fatigue life among others are enhanced. An increase in these properties is influenced by the optimization of process parameters.

2.4.1.2 Parameters influencing Laser Shock Peening Process

Desired results from LSP techniques involve optimization of processing conditions comprising mainly of laser and beam parameters, absorbent, and overlays. These process variables are used to control the depth, dislocation, surface characteristics and residual stresses imparted into the material. The process is optimized due to the interdependence of these process variables on each other such that the increase or absence either would lead to a less desired outcome. Therefore, these variables and conditions through studies are placed in ranges of each other to target materials to control the mechanical properties, microstructure, and residual stress profiles.

2.4.1.2.1 Laser and Beam Parameters

Typical requirements are placed on the Laser systems to achieve an effective LSP process. Laser systems used are usually required to be a pulsed system having an average power level ranging from 100 – 1000 watts, pulse energy of 10 J and above, and duration of 8 – 30 ns. Most commonly used laser system include the Q-switched and pulsed laser systems based on neodymium-doped glass or yttrium aluminum garnet (YAG) crystal lasing rod having wavelengths ranging from 1054 nm (infra-red), 532 nm (green), and 355 nm (ultraviolet) and pulse duration from 10 – 100 ns at 1- 100 J per shot [77]. Optimized wavelengths are important in achieving effective strengthening of metal samples by controlling beam interaction with the surface. The magnitude and depth of compressive stress induced in the material are proportional to the intensity of the beam controlled by the power density which depends on several process variables. At high plasma pressure, the power density increases and exceeds the material threshold to induce residual stresses with depth. Therefore, beam characterization is done to obtain laser intensity for the process. In pulsed laser systems, energy is delivered in a single train of pulses with a duration of fewer than 0.25s while Q- switched systems deliver flares of energy on a nanoscale duration. Shorter duration of pulses is found to generate a large magnitude of residual stress [78]. The energy (E) delivered by these systems is quantified as the peak pressure (P_{peak}) delivered per pulse time (P_t) or the average peak pressure (P_{avg}) delivered at a given frequency (f). This is expressed as;

Laser energy [78];

$$E = \frac{P_{avg}}{f} \quad (2.15)$$

$$E = P_{peak} * P_t \quad (2.16)$$

Due to the short pulse times of the laser, the energy wave to be delivered is grouped such that the duration lasts longer than 0.25s. This is known as *continuous wave* or *constant wattage (CW)* measured in Gigawatts per square centimeter. In this view, the term *power density* is used to describe the intensity (I) of the beam delivered on a laser spot area (A) and expressed with power increments as;

Laser intensity [78];

$$I = \frac{P_{avg}}{f P_t A} \quad (2.17)$$

Spot area varies depending on design and service conditions part material and may sometimes be overlapped until the desired effect is obtained. Several spot geometries including circular rectangular, elliptical, and square geometries have been studied to show that rectangular spots provide effective processing while square spots provide better uniformity and overlapping rate. When the laser beam is operated in a transverse electromagnetic mode (TEM), where the electromagnetic field is perpendicular to the optical cavity of a circular beam, the focal distance (F), beam wavelength (λ) and unfocused beam diameter (D) is related to the spot diameter (d) and is given by;

$$d = 2.44 \frac{F\lambda}{D} \quad (2.18)$$

From the laser diameter of the spot, the laser spot area (A) for the beam is calculated as $A = \pi d^2/4$. The depth of focus (DOF), greatly influences beam intensity by controlling the focal spot

size. A longer DOF is necessary for effective processing and this achieved by using shorter wavelengths with lenses of longer focal length. The relation between these parameters is given by;

$$DOF = 2.44 \lambda \left(\frac{F}{D} \right)^2 \quad (2.19)$$

The spot diameter has a great effect on the propagation of shock waves and its variation is limited by the power density and required laser power. Shock waves produced by a small beam diameter assumes a spherical shape. When impacted on the material surface, the shockwave attenuates proportional to the inverse square of the radius. But for large diameters of beam, the shockwave propagates to greater a depth by a planar-shaped shockwave. This results in reduced energy since attenuation is by the inverse of the radius. This observation concludes that residual stresses can be induced at greater depth with large spot diameter although the magnitude of surface CRS does not increase. An investigation by Masse and Barreau [79] showed that circular spots are not effective owing to the emission of focused waves from edges of the impacted area resulting in o residual stresses at the center of the treated area.

2.4.1.2.2 Transparent Overlay and Absorbent Coating

The protection of the metal surface during the process is required to prevent laser ablation and melting due to high power densities. Research studies showed that laser shock waves generated around $1GW/cm^2$ power density affects material thermal properties. Transparent overlays used in the process serves to confine the plasma on spot area of target by preventing the expansion of the plasma to surrounding material. The properties of the selected transparent overlay were observed to have a great influence on residual stress-induced. The parameters used in selecting the material for this purpose is based on density and acoustic impedance. A reduced shock impedance (Z) between the metal (Z_1) and the transparent overlay (Z_2) expressed by *equation (2.20)* is also used in the optimization of the process, was found to increase residual stress.

$$\frac{2}{Z} = \frac{1}{Z_1} + \frac{1}{Z_2} \quad (2.20)$$

The reduced shock impedance parameter improves the generation of shock waves and propagation into the material by increasing the laser intensity. Transparent overlays such as glass and water were found to increase the intensity of laser shock waves propagating within the metal sample by a second order in magnitude. Metal coatings such as aluminum, zinc, and organic coatings are mostly used as an absorbent coating to mainly protect the metal surface from melting and ablation but were found to also increase shock wave intensity. Research by Yu et al [80] showed a range where Laser power density (I) is influenced greatly by optimization of the transparent overlay and absorbent material from deformation to failure by *equation (2.21)* where the minimum pressure wave (P_{min}) necessary to induce the deformation must exceed the dynamic yield strength. A maximum pressure wave (P_{max}) was also found beyond which the rear face of the metal would break or lead mainly to material failure.

$$I_Y = 64 \frac{(\sigma_Y^D)^2}{MZA}, \quad P_{min} > 2\sigma_Y^D \quad (2.21)$$

$$I_U = 64 \frac{(\sigma_U^D)^2}{MZA}, \quad P_{max} < 2\sigma_Y^D \quad (2.22)$$

Where I_Y and I_U represent the laser power density at material yield and ultimate tensile strength respectively with a reduced shock impedance of Z . The absorption coefficient of the coating is given by A , with M as the transmission coefficient for transparent overlay. The dynamic yield

strength and ultimate tensile strength is denoted by σ_Y^D and σ_U^D respectively. Absorbent coatings and transparent overlays contribute mainly to changes in near-surface properties and microstructure. Successful LSP processing has been achieved in many works by combining water as a transparent overlay with black paint as the absorbent material [75].

2.4.1.2.3 Multiple Laser Shock Peening and Overlapping Spots

Target application methods can be used to influence the effectiveness of the LSP processing outcome. When residual stresses are induced in the surface of the material by impacting the same laser spot area successively with laser shots in the LSP process, the method is known as *multiple LSP*. This method of application is done to induce CRS at a greater depth than obtain by a single shot. The high number of shocks increases the magnitude of plastic deformation to material saturation. Although the outcome increases the residual stress in-depth, surface CRS is not enhanced by this method. This result was obtained from investigations on cast A356 alloy which had significant plastic deformation with the depth. Other materials showed different results. After three (3) impacts, the surface CRS was increased from 150 MPa at a single impact to 300 MPa for 7075-T7351 aluminum alloy. In a 0.55% carbon steel, the depth of CRS has increased from 0.9 mm to about 1.8 mm after three (3) impacts as shown in *Figure 2-7* below [75].

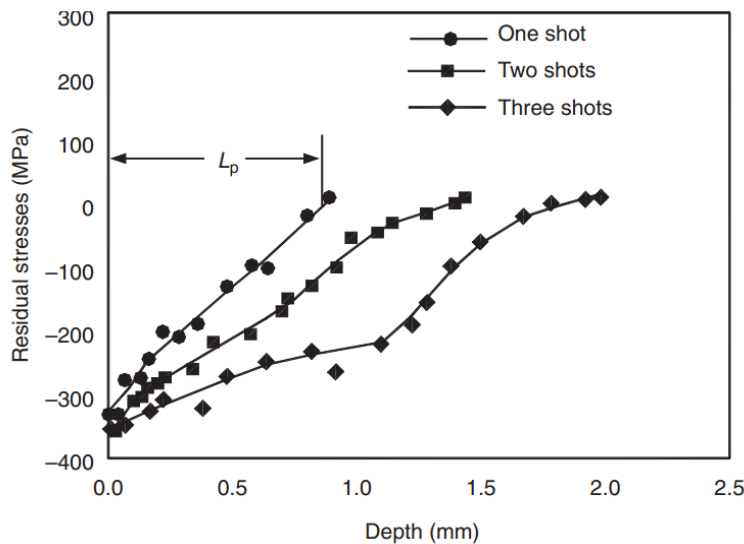


Figure 2-7. Depth of Residual Stress in 0.55% Carbon Steel by Multiple Impacts. [75].

Since many process variables are involved in effective LSP processing, residual stresses induced are not solely attributed to multiple impacts. Other methods such as spot overlapping are combined with multiple LSP to cover large areas of the part as well as optimizing the residual stresses induced. This is controlled by a factor known as the coverage ratio which gives a ratio of overlapping area to the impact laser spot size of two successive LSP processes [74]. The depth of plastic deformation increased by increasing the coverage ratio. This method is highly effective in removing the problems encountered with a circular laser spot by keeping the coverage area between 50 to 70%. In several applications, material degradation was reduced significantly by using the multiple LSP with overlapping spots produce uniform distribution CRS without inducing tensile residual stresses in overlapped regions. A study performed with 55C1 steel for four impacts with a laser diameter of 6 mm for 50% coverage ratio and a 25% overlap for 1 mm spot diameter at 50 impacts resulted in a reduced depth of plastic deformed region spot for smaller spot areas. The area of coverage is commonly used to improve the LSP process greatly for several industrial materials [77].

2.4.1.2.4 Specimen Geometry, Thickness, and Sided Peening

Many LSP studies carried out also showed the influence of specimen qualities such as geometry, thickness, and side of peening. Despite the technique being used in treating more complex parts, most studies focused on simple geometries such as flat surfaces where effects of variation and location of residual stresses can be observed. Challenges in complex geometries is an ongoing research area with some approaches from non-linear FEA studies. A study performed on AA7050 curved rods with diameters of the central sections as 4, 6, 8, 10, and 12 mm, using this approach showed radial and longitudinal inconsistencies in residual stresses owing to geometric constraint [81]. These observed variations tended to affect the desired property of the treatment. Due to large pressures involved in the treatment, the impact of the laser pulse is optimized based on the specimen thickness to avoid damage. Usually, to avoid distortion, CRS induced on the top surface of the specimen is reduced by 10% of the thickness as well as the number of impacts. These constraints are usually applied to thin specimen components. Thin specimens are usually

considered as thickness below 10mm which are mostly used for plate valves and gas turbine compressor blades. In the treatment of specimen of this thickness, great focus is placed on the effect of tensile stress which could lead to distortion or spall failure on the back surface. Therefore, the peening of thin sections is done in two different ways. One-sided peening usually requires rigid fixing of the specimen on a supporting plate while the exposed side is peened. This is done to use the supporting plate to resist the distortion seen as a dimple on the irradiated surface and bulge on the fixed side and to prevent spalling and fracture under strong shockwaves. Alternatively, both sides of the specimen are peened using a split laser pulse to balance out the generated forces. This method was to be unsuitable for complex geometries. There was no increase in depth of CRS, observed in an experiment conducted on 1.5 mm thick 4340 steel peened with five (5) shots but observed an increase in the magnitude of CRS. For thick sections, laser pulse may be applied simultaneously or individual at any spot on the material surface. The compressive zone in thick sections also increases with an increasing number of impacts without material distortion. This was supported by observation on a 10 mm thick AZ31B Mg alloy using one, two, and four laser impacts which depicted an increase in plastic deformation with increasing the number of impacts observed in compressive depth [47, 52].

2.4.1.3 Material Response to Laser Shock Peening Treatment

In research studies done to gain a better understanding of material response to LSP treatment, process parameters and conditions were evaluated to define the global influence of deformation of the target material as well as the residual stress profiles generated. Physical models were developed to analyze the elastic-plastic deformation induced by the laser shockwave. These models showed that the laser pressure pulse generated a purely uniaxial compression in the following the direction of the shockwave within the volume of the material to the ceasing point beyond which lies tensile stresses in the plane parallel to the surface of the target. Others showed that the nature of this deformation may also be influenced by the opposite side of treatment for longer plastic wave decay compared to the specimen thickness [82]. Compressive residual stress and strain hardening develop from plastic deformation of the material caused by the propagating shockwave. This, therefore, makes it necessary for the knowledge of the pulse pressure of the laser to control the

deformation. An elastic-plastic state is reached in the material when the *Hugoniot Elastic Limit* (HEL) is attained. This limit serves as the threshold where the material begins to classify and it occurs when the dynamic stresses of the propagating wave fall above the dynamic yield strength of the material. The dynamic yield strength σ_Y^D is related to the Huguenot elastic limit by *equation* (2.23), where ν is Poisson's ratio[75].

$$HEL = \frac{(1 - \nu)}{(1 - 2\nu)} \sigma_Y^D \quad (2.23)$$

Using this model, the plasma pressure at the interfaces between material and the transparent overlay is obtained to control and optimize both the physical and mechanical properties of the material from LSP treatments. Salimianrizi et al [83] demonstrated the effect on laser shock peening on the effect on aluminum and the number of compressive stresses generated. They saw that the yielding and microstructure reached depths of about 1873 μm beneath the material surface. The hardness of the material increased to this depth, which corresponds to a Vickers hardness between 120–145. The hardness was inversely proportional to the depth. Also, the roughness of the material was seen to increase. This showed that various outcomes can be expected from a treatment where several factors may be influenced positively or insignificant results could be obtained.

2.4.1.3.1 Residual Stress

One of the key desired outcomes of LSP treatments is the induced CRS because of its effects on material performance. It serves as resistance to applied tensile stress that minimizes fatigue and cracking of metal parts. Several factors influence the nature and magnitude of residual stresses impacted within the material. For treated samples, it is significant for the treated area to receive a relatively uniform distribution of stress, therefore experiments on spatial and temporal distribution of laser pulse pressure have been conducted to determine the variations in the magnitude of residual stress within the target material. Other factors influencing the outcome include absorbent

coatings, transparent overlays, number of shots, specimen thickness, overlapping spots, pulse wavelength, and duration and these play a significant role in the outcome such that it is difficult to pinpoint the exact influencing factor. The depth and magnitude of CRS depend greatly on laser power density given that the shockwave pressure is influenced by the intensity. Hence increasing intensity increases the depth and magnitude of the induced CRS. Limitation to increasing power density was observed at certain critical power density where micro-cracks are initiated resulting in damage [75].

Just like this limitation is the effect of pulse time. It was observed that longer pulse time tends to increase the depth of residual stresses but is restricted by melting and damage of both ablative layer and specimen. In an experiment conducted using power densities of 10 and 70 G/cm^2 with pulse times of 25 and 2.5 ns respectively for 35CD4 and XC38 steel, a compressed depth of about 1.55mm was by the largest CRS corresponding to the longer pulse time at lower power density. Laser wavelength was also found to increase top surface residual stress as it is increased [84]. A study on 6061 Al showed higher residual stress of -950 MPa for a 1064 nm wavelength and -750 MPa at 532 nm wavelength in 8 ns for 1.2 and 0.9 J/pulse power densities respectively. The presence of an ablative layer prevents the melting of surface which induces tensile stress on the surface of the metal with an insignificant amount of CRS. The use of this layer was found to increase the CRS surface of the material and mainly used to remove the thermal effect on the material. The effect of the layer is improved by the confining medium by focusing the shockwave to induce more plastic deformation but no studies have been found to support the effect of confining medium on residual stress profiles [81].

2.4.1.3.2 Microstructure and Surface Roughness

The evolution of the material during treatment would depict the material hardness and damage form the nature of dislocations induced by plastic deformation from high strain rates. This results in finer grains which enhances material properties such as tensile strength, hardness with improvement on fatigue strength. The maximum changes in the material are usually observed in the near-surface layer induced by the CRS in the plastically deformed region as it gradually decreases with depth and these are attributed to the laser process parameter and treatment

conditions. A reported study on AZ31B Mg alloy by Zhang et al [81] showed a result of finer grains from increased plastic deformation when the number of impacts was increased. Microstructure deformation near the surface is known to highly influence residual stress and serves as the fundamental to studying material strength modification. Most research on the effect of LSP treatment on the microstructure is mainly focused on the qualitative outcomes with minimum evidence on the quantitative feature mostly on the dislocation density.

Observation from surface analysis techniques used to illustrate changes of the roughness of material showed dimples on the treated spot which is characterized by an uneven surface. The quality of the surface roughness is mainly influenced by the magnitude of the laser energy and this quality is heightened when samples are treated without overlays. The absence of overlays influenced the changes in chemical compositions due to intense pressure and temperature subjected during treatment as material exposed to the mechanical and thermal loads. This results in the non-uniform surface layer with varied composition observed as a dispersion of smooth appearance and high-density pores. It was proposed from studies on various steels that the high-density pores were due to the formation of an oxide layer in regions of a high content of chromium and oxygen and smoother areas occurred after melting and re-solidification of the surface layer. One particular study of a steel sample showed a thickness of 5 -15 μm of melted layer and 1 – 2 μm thickness of the chromium oxide layer. [85]. Other studies confirmed that higher roughness can be achieved by higher laser power density when a 2205 duplex steel was used without overlay as well as increased exposure time at constant pulse energy would result in a higher scale of roughness. Shadangi et al [86] conducted tests to access the effect of the exposure time on the average surface roughness. Five (5) samples were treated with exposure times from 0 – 20 min with 5 min. the average roughness increased as 0.046, 0.127, 0.154, 0.340 and 0.367 μm respectively. Similar results were also discovered when overlapped spot increased the roughness with the average roughness of 0.568 μm was recorded for 5min exposure time attributed to high-density dislocations.

2.4.1.3.3 Hardness and Yield Strength

The surface hardness of the material is translated from the *microhardness* or *nano-hardness* of the laser-treated spot. The LSP process conditions, type of alloy, and the microstructure are optimized to increase the surface hardness. The magnitude of surface hardness diminishes with depth from the laser spot. This quality is found to be different over regions of the irradiated spot. LSP is used to improve microhardness as deformation is induced on impact causes material to reinforce work-hardening effects observed as the increase in microhardness. Process parameters such as power density, overlapping spot, number of impacts, and peak pressure influence the hardness magnitude. A study performed on Ti-6Al-4V alloy with 40% overlapped spots showed a 15% increase in hardness for a single shot and 24% for a double shot. It was also evident that sufficient energy is required to increase dislocation density which causes an increase in the microhardness. For treatment on AISI 4140 sample, the highest hardness was reported at 2.4 GW/cm^2 and 4 GPa for power density and peak pressure respectively as shown in *Figure 2-8* below. An increase of 20% in the hardness was also reported with spot treatment for 2 hours. Beyond this value, a decrease in hardness was observed due to over tempering after two (2) more hours [81].

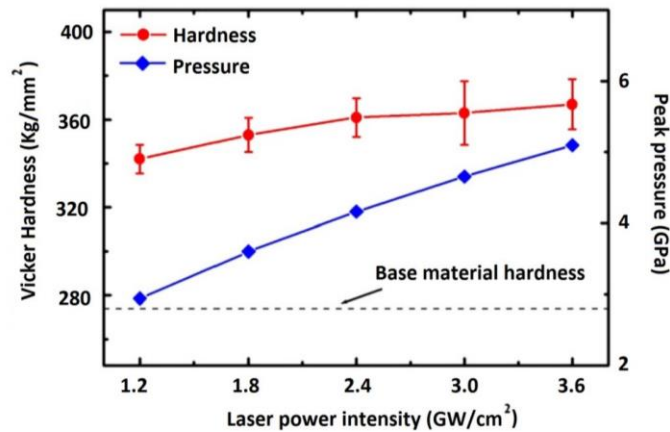


Figure 2-8. Surface hardness for AISI 4140 and Corresponding Peak Pressure [74].

Similarly to surface hardness, the yield strength is increased by the LSP treatment, although the level of increase is sometimes impeded by the type of material and was attributed to inelastic strain

due to shock and the distribution of in-depth compressive residual stresses as reported by the treatment of aluminum alloys by Fairand and Clauer [81]. Higher dislocation density initiates the increase yield strength as well as the CRS distributed and this was supported when a 50% increase in tensile strength for 6061-T6 aluminum alloy and 60% in yield strength for friction stir welded (FSW) joint of Al2195 after LSP treatment was recorded [75].

2.4.1.3.4 Fatigue Life

The development process of the SP treatment technique was based on the improvement of the fatigue life machine components by controlling the onset and propagation of cracks. LSP technique has shown great improvement in fatigue life of blades and generally the mechanical properties of most alloys by fatigue strength enhancing. Other material properties also tend to influence the fatigue life. LSP processing parameters are used to increase the fatigue life of most materials with initial studies focused on the effects of different shapes of laser spots. Two types of laser spot used to treat regions of a 2024-T3 aluminum alloy specimen with notches and cantered hole, reported an increase of the fatigue life by 40 times, for a solid laser spot compared to the non-shocked region while annular-shaped configuration produced 3 times the fatigue life of the non-shocked ones. Furthermore, the experiment proved beneficial effects increasing the resistance to pre-existing cracks where the solid laser spot had the lowest crack length and non-shocked the highest [75]. In the LSP experiment conducted by Zhang et al with a 40% overlapping spot at 370 MPa peak stress, an increase in the number of impacts was observed to increase fatigue life by 22.2% and 41.7% for one and two shocks, respectively. Additionally, a decrease in fatigue life was observed with increasing the number of shocks and was ascribed to instability in the CRS, stress concentration, overlapped shocks, surface roughness, and the destruction of the absorbent layer as shown in *Figure 2-9* below.

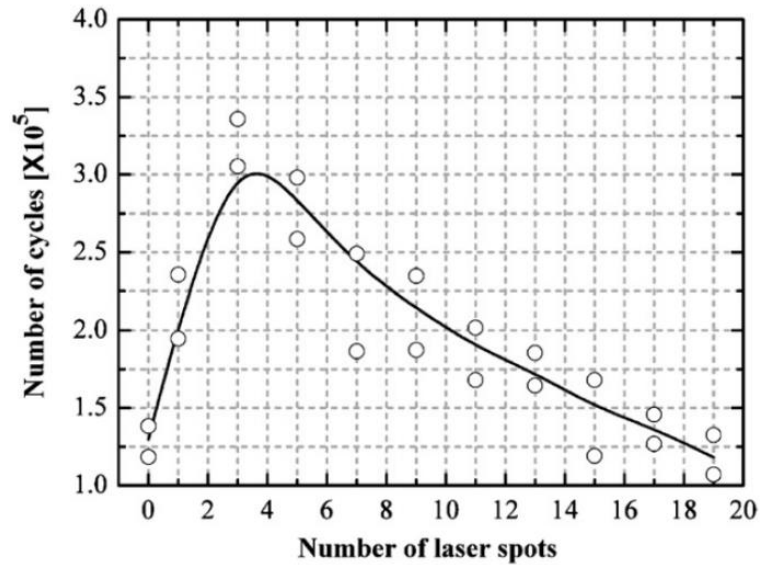


Figure 2-9. Effect of Number of Laser Shocks on Fatigue Life for Ti-6Al-4V Alloy [74].

2.4.1.4 Characterization of Laser Shock Peened Materials

The desired changes that accompany LSP treatments are observed, quantified, and evaluated using various measuring methods that are usually specific to the expected property. Most desired properties border on the residual stress, microstructure, and mechanical properties such as hardening, strengthening, and roughness of the material. Changes occurring in the microstructure of the material can be investigated and characterized using SEM, TEM, and Profilometer. *Transmission Electron Microscopy* (TEM) is used mainly to analyze the grain structure by dislocation structure, dislocation entanglement dislocation band, and precipitate structure. The distribution and density of both fine and coarse nano-particle changes can be detected using this method. Surface profiles depicting roughness, curvature, and general topography of the material is analyzed using *Profilometer*. The most used are optical methods including interferometry and confocal microscopy. These produce peaks and valleys in the surface profile which is magnified to obtain and quantify the roughness. Roughness or micro indents observed can be areas for stress concentration which is used to determine fatigue of material Surface morphology and irregularities produced from LSP treatments can be investigated using *Scanning Electron Microscopy*. This method characterizes both surface and sub-surface features which are used in some fatigue analysis

of materials. Features such as cracks and fretting, mild indentations, and melting that may occur due to ablation are detected [81].

Hole drilling, X-ray diffraction $\sin^2\psi$, slitting, neutron diffraction, and contour methods are the most common ways of evaluating residual stresses. The effectiveness of the LSP treatment depends greatly on the induced residual stresses. This property is quantified using stain in the crystal structure while considering a linear elastic deformation in the crystal lattice. In X-ray diffraction $\sin^2\psi$, material constants such as Young's modulus, Poisson's ratio, and tilt angles are used to obtain strain that quantifies residual stresses. The hole-drilling method uses the strain gage rosette to measure the variations in stress as a function of depth as the hole is created into the treated material. Plastic deformation during the process results in dislocation motions which attribute to an increase in hardness. Levels of material hardness are determined by various test methods. Using the Vickers hardness tester would quantify the bulk hardness of the treated sample. Microhardness and nano hardness can also be detected using micro and nano testers. These are more suitable in quantifying the hardening induced from the strain [52,53].

2.4.1.5 Laser Shock Peened Materials

LSP technique has been used on different types of material for various applications with specific desired properties relating to residual stresses, stress and corrosion cracking, mechanical properties, and fatigue behavior as well as the alteration in the microstructure. Most of these materials used include a whole range of metal alloys of zinc, nickel, aluminum. Steel and titanium amongst others and bulk metallic glass. Most LSP research performed with metal alloys compared the variations in mechanical properties based on the optimized process parameters while others compared the improvement of material properties by LSP techniques to shot peening. In the table below, remarks from various research on different metal alloys and their process parameters are shown

Table 2-1. Comment on LSP Treatments of Different Materials Obtained from Literature

Material (Reference)	Power Density (GW/cm²)	Pulse Duration (ns)	Remarks
AISI 347 Activated flux TIG weld [87]	5.97 2500, 5000, 7500 pulses/mm ² No coating	10 Spot diameter - 0.8 mm No overlay	LSP without coating showed higher CRS with better mechanical properties. Higher average hardness was displayed for pulse density of 5000 pulses/cm ² with multiple shots. Above 5000 pulses/mm ² , thermal damage occurred resulting in reduced hardness.
Modified 9Cr-1Mo (P91) Steel [88]	3.9, 4.7 & 5.5 Coating - black PVC tape	9 Spot diameter - 3 mm Water overlay (2 mm thick)	CRS increased substantially from 85 MPa for the untreated state to 580MPa for LPD of 3.9 GW/cm ² and a subsequent marginal increase to 620 MPa for 5.5 GW/cm ² LPD keeping all other parameters constant. The microhardness was increased by 20 - 27% for single, double, and triple peening using a constant LPD of 3.9 GW/cm ² .
AISI 304 stainless steel. [89]	5, 10 & 15 5, 10, 25 pulses/mm ² Coating - Foils (AL, Fe & organic black paint)	8 Spot diameter - 1-2.5 mm Water overlay	Optimal Laser intensity was obtained at 10 GW/cm ² for maximum surface hardness increase by 53% at 25 pulses/mm ² . Corrosion rate and wear volume were decreased by 86.7 % and 50% respectively contributing to enhanced fatigue life.

Ti-6Al-4V alloy [90]	5 Coating - 7050 Aluminium foil	10 Spot diameter - 5 mm Water (2 mm thick)	Fatigue life increased to a maximum before decreasing with an increasing number of overlapped spots. CRS was distributed relatively on the irradiated surface and decreases with depth and translates into tensile stress.
6082-T651 Al alloy [91]	10.75 900 & 2500 pulses/cm ² No coating	10 Spot diameter - 1.5 mm Water overlay	The better surface condition was displayed by laser with 900 pulses/cm ² in both transverse and longitudinal directions. Both pulse densities, from micro-hardness depth profile, confirmed an increase with 800µm depth of impact of shock waves.
2024-T3 Al alloy [92]	5 Coating - Black paint	18 Spot diameter - 10 mm Water overlay	A significant increase in fatigue crack life and fatigue life was observed to be higher than untreated samples but decreased with an increase in stress concentrations around notch root. The lower magnitude of crack growth rate was observed for LSP samples.
TC11 Ti alloy [93]	11.2 Coating - Aluminium tape	10 Spot diameter - 3 mm Water overlay (1-2 mm thick)	Remarkable tribological properties were recorded for LSP treated samples due to high CRS and grain refinement induced by the process. Lower wear rates were displayed by the LSP treated samples compared to untreated samples.

<p>1045 Medium carbon steel [93]</p>	<p>1.68, 3.46, 4.4 & 6.0 Coating - Black tape</p>	<p>5 Spot diameter –1.5 mm BK7 glass overlay</p>	<p>Low laser intensities result in a decrease in coefficient of friction (COF), while surface strengthening effects reach a peak point at higher intensities Laser intensity can be optimized to obtain a decrease of 17.5% - 83.25% in the COF depicted by 4.4 GW/cm² and 6.0 GW/cm² recording 0.067 and 0.112 COF respectively</p>
--	--	--	---

2.5 CAVITATION EROSION ASSESSMENT METHODS

This major section introduces standard techniques used in laboratories to induce cavitation for studies and the methods used to evaluate the magnitude of cavitation damage. *Section 2.5.1 laboratory techniques*, presents two major standard techniques; vibratory cavitation and cavitating liquid jets apparatus used to create erosion damage. *Section 2.5.2 cavitation erosion progression*, introduces the periods during cavitation erosion progression and the measurement methods used to analyze the magnitude of damage by cavitation.

2.5.1 LABORATORY TECHNIQUES

Experimental studies performed in the laboratory provides a comprehensive means of validating the performance of new materials. Laboratory tests are accelerated tests to achieve results within a short period. Hence, to understand and predict the performance of materials in cavitating flow fields, laboratory cavitation tests are performed to emulate field erosion tests to anticipate the conditions for the damage as well as quantity and quality of the damage. These tests are aimed to establish relations between the erosion damage, the magnitude, and frequency of cavitation on a material surface. Various techniques for evaluating cavitation erosion include rotating discs, submerged cavitating jets, ultrasonic vibratory devices, and cavitation flow loops focused on generating cavitation bubbles and erosion resistance. Amongst these are standardized tests that follow the American Society for Testing and Materials (ASTM). The vibratory test method (ASTM G-32) and cavitating liquid jet method (ASTM G-134) are discussed in detail [94].

2.5.1.1.1 VIBRATION CAVITATION APPARATUS (ASTM G32)

This is a rapid small-scale method for analyzing cavitation erosion resistance. This method of generating cavitation is different from flowing systems such as the cavitating jets, but produces the same results. This method exposes the material surface to controlled, intense repeating stress cycles capable of inducing significant surface erosion in a short period. The set-up comprises a

vibrating device that uses sonotrode (*ultrasonic horn*) *staked* with a transducer capable of undergoing expansions and contractions to produce ultrasounds when supplied with an alternating electric field. The test specimen is usually attached to the tip of the sonotrode immersed in a beaker filled with test liquid (generally de-ionized water) and surrounded by a cooling bath. Oscillations produced from the vibratory motions of the sonotrode deliver cyclic pressures at a high frequency of about 20 kHz.

This is enough to create high negative pressures capable of breaking tensions in liquids to induce cavitation bubbles. Experiments performed gave different results with test material placed directly on the sonotrode and at a varied distance which gave rise to two methods (*see Figure 2-10*) of irradiation. The direct method differs from the indirect method as it uses a cavitation resistant sample (dummy button) fixed directly on the sonotrode tip with test specimen below at some defined distance as shown in the figure below. A significant difference in patterns was observed for both methods [95]. The direct method showed a more concentrated erosion around the center of the test material while the indirect method showed a more spread out erosion. These observed patterns were attributed to bubble collapse patterns near the test specimen. Bubble collapse under the direct method was observed to collapse in a hemispherical pattern towards the test sample with the indirect method, collapse is in a cylindrical pattern. Test conducted on Al 7072 samples using both methods showed a slower material erosion progress for the indirect method as compared to the direct method. A relation between cavitation intensity and displacement amplitude showed that a reduction in frequency and amplitude resulted in reduced erosive effect [96]. The ASTM G32 tests are very common due to its effectiveness and reproducibility of cavitation in laboratories with bubbles of approximately uniform sizes under the fixed frequency of the horn. It varies from real cavitation fields which produce bubbles of various sizes under different exciting frequencies and shows inconsistencies due to the constant location of bubble cloud.

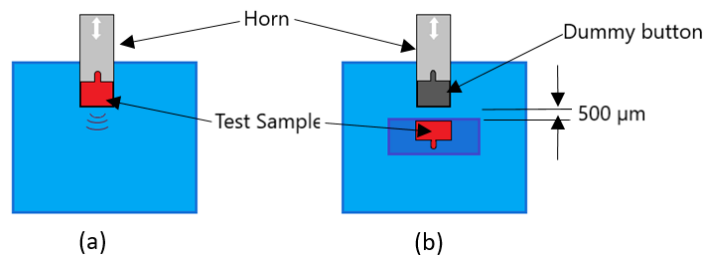


Figure 2-10. Direct Method (a), Indirect Methods of Vibratory Cavitation Apparatus (b). [95]

2.5.1.1.2 CAVITATING LIQUID JETS (ASTM G134)

The cavitating liquid jet method was first introduced by Lichtarowicz et al [97] to assess the cavitation intensity of submerged liquid jets by controlling the type of a nozzle, jet velocity, the jet diameter as well as standoff distance between the nozzle and the specimen. The test method design by Lichtarowicz is called *Lichtarowicz cell*. Since this method provides a flexible way of studying the cavitation intensity by varying various parameters, the method is employed as a standard for evaluating the effects of material property by cavitation. Test conducted through this method by Momma et al [52] on PVDF (polyvinylidene fluoride) on a film gave similar results as other cavitating test methods but provided more accurate practical results with the various size of microbubbles, shear flows with vortices, and dense bubble clouds, which collapse on the sample. When the pressure difference is applied across devices like nozzles, any submerged liquid jet would cavitate along the smallest diameter, with bubble collapse occurring along the throat of the nozzle and down the stream.

The scheme designed to consist of two flow controlling loops sharing a pump. The first loop circulates water through the left side of the pump. It consists of a cavitating nozzle, as a sample holder, and a test chamber with ambient pressure. The sample holder has a fixed position which allows the running test to be stopped and continued at any time by removing the holder and placed back at the precise location. The second flow loop circulates test liquid through the right side. It is made up of a cavitating nozzle with an orifice diameter of 0.4mm conforming to G134 specification, a sample holder, a pressurized test cell, a water reservoir, and the pump [95]. A schema of the test chamber is shown in *Figure 2-11* below. During testing, a high capacity pump is used to discharge test liquid through the nozzle of variable throat diameter. The pressure of the upstream flow into the nozzle is noted as P_{jet} and P_{tank} as the downstream flow within the test section. The distance between the nozzle throat and specimen is known as the standoff distance, used to control the spread of the jet on the material surface. Test liquid is then removed from the test section through the outlet valves.

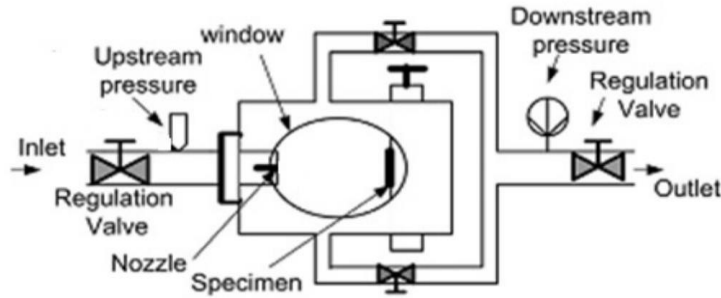


Figure 2-11. Test Section of Cavitation Liquid Jet Apparatus. [98]

Studies performed showed the influence of nozzle geometry on cavitation parameters such as downstream pressure, jet velocity, and pressure distribution in the test chamber. A decrease in nozzle diameter results in a decrease in the jet width, jet spreading angle, and cavitation cloud density. Lichatarowicz observed that smaller throat diameters such as 2mm can achieve pressures close to 450MPa with a jet velocity of 250 m/s. One important parameter influence used in cavitation jets is the cavitation number. Hutli et al [98], investigating the effects of nozzle geometry on the erosion process concluded that cavitation intensity and distribution and strength of the bubbles, as well as the penetration of the jet and the jet spreading angle, are strongly influenced by cavitation number. Consequently, a decrease in cavitation number increases the mass loss, the erosion rate, and the eroded area. They also found out that nozzle geometry dominates all other parameters. Cavitation number is applied mainly in open flow systems as well as constricted channels such as nozzles and is dependent on the ratio of flow velocities and pressures in cavitation regions. In erosion testing, where jets and samples are submerged in water tanks and exposed to the atmosphere cavitation number is dependent on cavitating jets by the ratio of pressures expressed in *equation (2.24)*.

$$\sigma_{jet} = \frac{P_{tank} - P_v}{P_{jet} - P_{tank}} = \frac{P_{tank}}{P_{jet}} \ll 1 \quad (2.524)$$

Where P_v is the vapor pressure of the liquid, which is insignificant because $P_{jet} \gg P_{tank} \gg P_v$ and the relation can be simplified as shown in the equation (4.24), above.

2.5.2 CAVITATION EROSION PROGRESSION

In hydrodynamic operations, mechanical properties of materials such as hardness, roughness, and tensile strength are of great importance in evaluating impact loads leading to cavitation damage and moderating levels of failure. The relation between the hardness and tensile strength of materials is used to describe the physical properties. Tensile strength describes the highest possible impact a material can resist before rupture while hardness measures the material resistance to surface indentation. Various tests performed on material showed a linear relation between hardness and tensile strength with dependence on the type of hardness scale used. Conversely, surface roughness has a strong effect on the hardness of the material and influences the nature of deformation and measures the wear and friction. Analysis of these quantities can be performed through the various test with a focus on the magnitude of cavitation damage on surfaces. Cavitation effects on the mechanical properties of materials are realized during the collapse of bubbles influenced by the operating conditions surrounding the material. Cavitation erosion process yields different features for a given exposure time. Hence the erosion rate is classified into four stages as shown in *Figure 2-12* by the characteristic cumulative curves of mass loss rate versus exposure time.

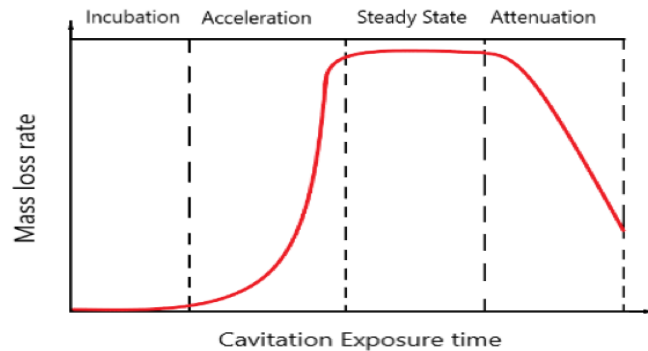


Figure 2-12. Characteristic Curve of Erosion Rate Versus Exposure Time.

2.5.2.1 INCUBATION PERIOD

The resistance of a material is usually associated with the period of incubation. During this period, cavitation shotless peening is observed and erosion rate is considered negligible compared to other stages since there is no significant mass loss. The impact from bubbles here causes plastic deformation to material by introducing compressive stresses with resulting smooth profile of pits. This stage is of great importance in research studies of metals especially alloys where shockwaves produced are stacked into faults resulting in a longer incubation period and thus, enhanced cavitation resistance [99]. The length of the incubation period is a necessary factor in estimating the lifetime of the material. Mass loss of metal surface is observed physically by the formation of pits. Pits formed, provide a positive definition for estimating cavitation intensity, different material response to various impact loads, and the effect of fluid type on erosion damage.

Pitting tests are popular in evaluating the onsets erosion damages. Although pitting technique is still under investigation to quantify cavitation intensity from impact loads, it is assumed that, during the incubation period, the formation of a single pit is produced by a bubble collapse near the wall. Various experimental devices used in pitting techniques produce a large spectrum of bubbles with different sizes at different distances which poses a major problem in characterizing the individual erosive potential of each bubble due to interaction with other bubbles in the vicinity. Improved results for controlled tests which produce consistent bubble characteristics, only has a downside of not corresponding to real cavitation fields.

Cavitation pitting contributes greatly to fatigue in hydraulic components with pits ranging with different sizes and shapes from a pinhead to spherical that can penetrate several inches of the thickness of the metal surface enough to fail. Cavitation pit deformation is usually characterized as a segment of a sphere with a deep central portion and flat portion on both sides by the pit diameter ($2a$) and depth (h), as shown in *Figure 2-13*.

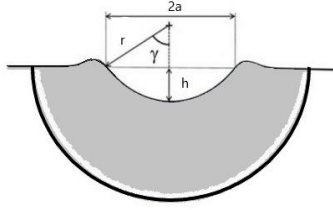


Figure 2-13. Depicting Theoretical Cavitation Pit.

Due to the structural orientation of materials, pit shape is dependent on the plastic deformation which assumes the cavitation bubble as a spherical indenter to generate a mean strain (ε) expressed as;

$$\varepsilon = k \sin \gamma \cong 0.2 \left(\frac{a}{r} \right) \quad (2.525)$$

Where k is a coefficient for spherical indent approximated to 0.2, γ is half the angle made on contact and r , is the radius of the sphere which is geometrically related to the pit depth and can be expressed as;

$$r = \frac{a^2 + h^2}{2h} \quad (2.526)$$

$$\frac{h}{a} = \frac{1}{\sqrt{(2r/h) - 1}} \quad (2.527)$$

This relation can be modified as shown in *equation (2.27)* to obtain a geometric term, h/a , known as the shape factor which depicts how stress is concentrated onto the surface and hence indicating the initiation and direction of crack propagation leading to material failure.

During the incubation period, pit analysis is necessary to obtain information about the behavior of a material and to create erosion prediction models that best describe the stages in cavitation erosion. These analyses include the counting of pits which was proposed to depict the initial formation of permanent plastic indents without mass loss, owing to the impact energy of collapsing bubbles. The formation of the pits characterizes the final deformation before the effects of fatigue are significant [100].

The distribution of pits formed does not show a uniform distribution of cavitation filed due to random bubble impacts. Since the size of the pit is significantly small, the probability of overlapping is considered negligible and flow aggressiveness can also be predicted during the incubation period, A detailed analysis of pitting tests discovered that the smaller the pits the higher the pitting rate. The Weibull distribution was proposed for a non-dimensionless pitting rate which showed a relation between the normalized pitting rate, \bar{N} and the normalized pit diameter, \bar{D} as;

$$\bar{N} = e^{\bar{D}^{k_w}} \quad (2.528)$$

$$\bar{N} = \frac{N}{N^*} \quad \text{and} \quad \bar{D} = \frac{D}{D^*} \quad (2.529)$$

Where N , is the pitting rate, N^* , is the characteristics pitting rate derived from statistical values of pit formation a characteristic pit diameter D^* and D , is the pit diameter. The surface area is more influenced by pits with sizes greater than D^* but have less occurrence as compared to pits with sizes smaller than D^* . Pits can be realized through several methods including contact profilometry, Scanning Electron Microscopy (SEM), optical profilometry and laser profilometry, optical interferometry.

2.5.2.2 ACCELERATION, STEADY-STATE AND DECELERATION PERIODS

Significant mass loss is measured from the acceleration stage to a maximum rate level. During this stage, cavitation intensity increases, and more pits are formed contributing to a weight loss of material. The nature of boundary flow is changed by this, resulting in fluctuations in pressure fields since the surface is covered with pits and microscopic cracks. The onset of material rupture occurs in this stage. The acceleration stage is followed by a steady-state region where erosion rate is almost constant representing a balance between the erosion intensity and material response. Cracks formed at the grain boundaries evolve into deep craters. These craters tend to trap the fluid which acts as a damper to pressure peaks between the material surface and collapsing bubbles [101].

As surface properties changes, especially roughness due to the formation of more pits and craters. Bubbles collapsing near the vicinity of the surface do so at decreased pressure and this results in reduce erosion rate observed in the attenuation stage by the decelerating curve [102]. The deceleration approaches a pseudo- constant value depicting a balance between the acceleration and attenuation stages for constant flow field conditions and insignificant changes in material geometry. During the evaluation, the eroded profile of material can be plotted for different exposure times to obtain the maximum erosion depth to estimate the cavitation resistance of the material. The erosion time history is of most ductile materials is depicted by an S-curve which shows no mass loss during incubation time T . This is characterized by a normalized volume equation by;

$$\bar{V}_{loss} = 1 - e^{-\bar{t}^n} + \alpha \bar{t}^\beta \quad (2.530)$$

$$\bar{V}_{loss} = \frac{V_{loss}}{V_{loss}^*} \quad \text{and} \quad \bar{t} = \frac{t-T}{t^*} \quad (2.531)$$

The values of V_{loss}^* , t^* and T are the characteristic values depicting the material response in the flow field. The values of α , β and n are parameters that characterize the erosion and are obtained

from the cavitation database based on the erosion apparatus used. taking the second derivative of with time gives the characteristic time, t^* which defines the time taken to reach the maximum erosion rate. This can be used to evaluate cavitation intensity and pressures.

2.5.2.3 EROSION MEASUREMENTS

There are a series of measurement methods used to evaluate erosion parameters such as mass loss, volume loss, pit depth, and diameters, impact pressures, and flow velocity. The mass loss method is usually associated with ASTM G32 vibratory apparatus. It is obtained, simply by weighing the sample at various time intervals to predict the erosion progress. This method creates an indistinct difference between the cavitation and the environmental effect. The volume loss method is usually preferable when the changes in the mass are difficult to obtain.

During the tests, using the mass loss method, the total cumulative mass loss, $M(mg)$ is determined by the intermediate-mass loss, Δm_i at each time interval by the relations;

$$M = \sum_{i=1}^n \Delta m_i \quad (2.532)$$

$$\dot{M} = \Delta M_i / \Delta t_i \quad (2.533)$$

Where Δt_i , is the intermediate time (min), attesting period, i , and \dot{M} , is the erosion of mass loss rate during the period (mg/min) and n is the number of tests performed.

The material resistance to cavitation can be evaluated by the depth of erosion and the rate of erosion depth. This is used to indicate the impact of cavitation to sample surface. According to ASTM G3-2010, the mean depth erosion, MDE (mm) and mean depth erosion rate, MDER (mm/min) is related by;

$$MDE_i = \sum_{i=1} \Delta MDE_i = \frac{4 M_i}{\rho \pi d_c} \quad (2.534)$$

$$MDER_i = \Delta MDE_i / \Delta t_i \quad (2.535)$$

Where ρ (g/mm^3), is the density of the material and d_c , is the diameter of the exposed surface to cavitation.

Deformation in the material surface can be measured by a profilometer to exhibit the relation between material behavior with erosion. The profiles may be obtained in 2D for a well-defined cavitation field. the use of contact profilometry methods is limited by the radius of the stylus tip. The profiles obtained can be filtered with standard roughness cut-offs to define peaks and radius of unmerged pits. The results of this method can be validated using microscopy methods to evaluated the depths in the exposed field.

3 EXPERIMENTAL DESIGN AND MEASUREMENT

In this chapter, the goals of this investigation are elaborated in *section 3.1* and the experimental setup and operation principle are described in *section 3.2*. The measurement procedure and standards used to generate cavitation erosion are presented in *section 3.3*. *Section 3.4* presents the specimen material used with both the chemical composition and mechanical properties. The specimen dimensions and masses are also given.

3.1 EXPERIMENTAL GOALS

The study of this work contributes to the knowledge of the selection of surface modification treatment for materials for hydraulic components to give better resistance to cavitation damage. This study evaluates whether LSP treatment is a better and advanced modification technique to be employed in the design of components parts to improve the resistance to cavitation erosion and enhanced fatigue life.

The main goal of this experiment is to evaluate the effect of LSP treatment on material resistance to cavitation erosion of an LSP treated steel type used for pump blades and to compare the resistance to the untreated steel type material and compare the effect of the process parameters on the resistance to cavitation erosion. The aim is to conduct mass loss measurements in the laboratory using the ultrasonic vibratory apparatus and results reported in terms of the periods depicted by the erosion -time curves by the volume loss and rate of volume loss. The secondary goal was to compare the erosion depth with the depth of residual stresses induced in the sample during the LSP treatment and evaluate which treatment process parameter resulted in higher resistance.

The sample was prepared using the LSP technique. The samples were subjected to different process parameters. The cavitation erosion of the sample material was compared to samples from earlier experiments with equivalent results to estimate the incubation time of the present samples. The interest compares the same steel types of different treatments.

3.2 EXPERIMENTAL SETUP DIAGRAM

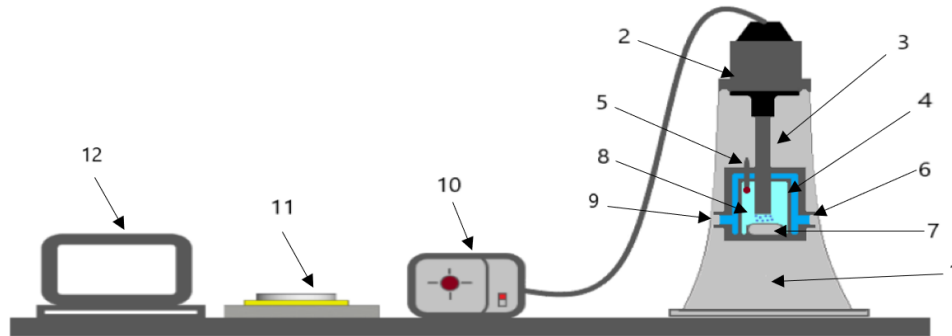


Figure 3-1. Illustration of Experimental Setup for Cavitation Erosion Test.

1 – Test Stand; 2 – Transducer; 3 – Horn; 4 – Cooling Bath; 5 – Thermometer; 6 – Inlet; 7 – Test Specimen; 8 – Distilled Water; 9 – Outlet; 10 – Ultrasonic Generator; 11 – Mass Balance and 12 – Computer.

As shown in *Figure 3-1* above, the system comprises ultrasonic vibratory apparatus which is powered by the ultrasonic generator with an amplitude regulator. The temperature of in cavitating chamber is checked and controlled by the thermometer and cooling bath respectively. The mass loss after each time interval is measured with mass balance and analyzed with a computer.

The ultrasonic vibration cavitation system (UVCS) is the vibration device used to induced cavitation on materials in the laboratory for cavitation experiments. The system is used to overcome the time constraint experienced in actual cavitation erosion test in equipment by exposing the material to controlled repeated, intense stress cycles resulting in significant erosion in a short period [84]. *Figure 3-2* depicts the main components and principles of operation of the system.

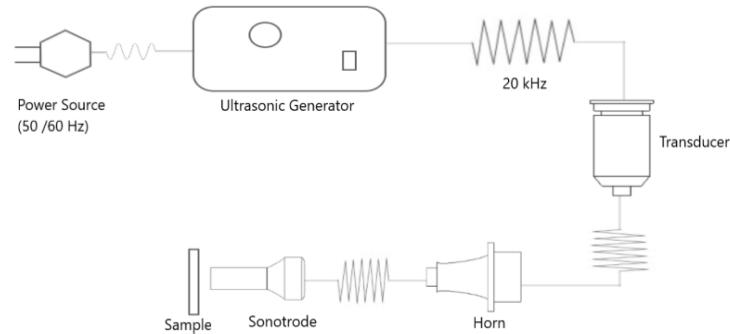


Figure 3-2. Components and Principle of Operation of UVCS.

The whole system is electrically powered by the ultrasonic generator. This component receives an electrical signal from the power source usually with a frequency of 50 Hz or 60 Hz and converts from a lower voltage to a significantly higher voltage with a specific frequency usually at 20 kHz, essential to induce cavitation and the signal is supplied to a converter. The ultrasonic transducer acts as the convertor and transmits an electrical signal into an ultrasonic signal by the piezoelectric effect. The horn in the system is a metal rod with a round cross-section that displays the mechanical amplitude displacement received from the transducer. Attached to it, is the sonotrode with stacks of piezoelectric crystals at the tip which transmits ultrasonic waves into the liquid causing the formation of cavitation cloud and dynamics at the sonotrode tip which proceed to collapse bubbles resulting in cavitation erosion.

3.3 PROCEDURE FOR CAVITATION EROSION TEST

The test was performed using the recommended standards ASTM G32 described in *Table 3-1*. The standards encompass a set of relatively simple and controlled tests to produce cavitation damage and material loss on the various material specimen. In the setup, the transducer is attached to the horn which generates an amplitude of up to 20 kHz frequency. The horn is positioned closed to the surface of the sample to allow maximum amplitude oscillations. Due to standard requirements, a gauge block is used to set the gap distance between the tip (sonotrode) and the sample by controlling the height of the sample holder which completes the base of the cavitation chamber by screw attachment.

In preparation for the test, the sample is cleaned with alcohol and distilled water to remove the formation of an oxide layer on the surface. The sample was then fixed into the sample holder by a definite position and attached to the cavitation chamber which also houses the horn. The definite placement of the sample in the holder is done to purposely control and obtain a consistent cavitation field on the sample surface. The chamber is filled with distilled water and a temperature sensor is placed within to monitor the temperature changes in the test liquid. Tap water, used as the cooling bath for the test is controlled through the inlets and outlet of the chamber to control the temperature of the test liquid during the operation.

The exposure time of the sample to the cavitation bubbles was timed with the power of the ultrasonic generator. The experiment is designed to with intervals of 30 min to observe the initial mass loss and subsequently increased to 60 and 120 minutes to observe the mass loss over large periods. During the exposure, the temperature is maintained about 25 ± 2 °C with 100% vibration amplitude. After the assigned time interval, the generator is powered off and the sample is removed and dried for about 3 minutes to remove moisture and the mass is recorded. The subsequent analysis is carried out in the same procedure.

Table 3-1. ASTM32 Recommended Standards for Cavitation Tests

PARAMETER	VALUE	UNITS
Frequency of Vibration	20 ± 0.2	kHz
Vibration Amplitude	57	μm
Gap Between Horn and Sample	5	mm
The temperature of Test Liquid	25 ± 2	°C

3.4 MATERIALS DESCRIPTION

The material of LSP treated samples used in this study was SS304 stainless steel alloy supplied as a cylindrical block with 49.8 mm diameter and 10.98 mm thickness shown in *Figure 3-3* by 2D drawing. The pattern created by the treatment is also shown. The samples were cut and prepared by the materials department of Hilase Center. This material contains chromium and nickel as the base constituents and is highly resistant to pitting corrosion and erosion than regular steel and has a density of 8000 kg/m³. The typical chemical composition (in wt. %) and mechanical properties of SS304 alloy are listed in *Table 3-2* below. Both samples were treated on a single side with 14 ns pulse length at 10 Hz repetition rate and 50% overlap. The LSP treatment of the samples was carried out using a 2 mm thickness of water as a confining medium and black tape for ablation protection. The different processing parameters for both samples are also listed in *Table No.* as well. An untreated sample of SS304 is used as the reference specimen for the test.

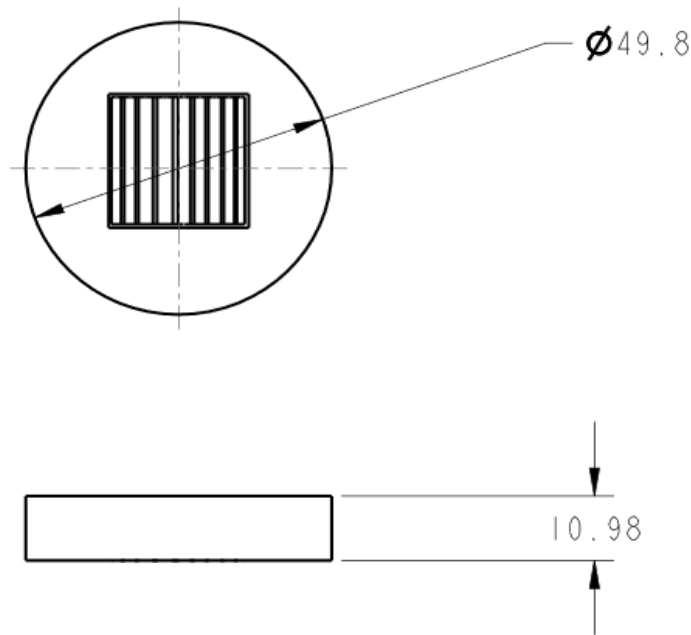


Figure 3-3. Dimensions of the test sample for erosion test

TABLE 3-2. Chemical and Mechanical Properties and LSP Process Parameters of Samples

Code	Chemical Composition								
Reference, S/3/3 and S/6/3	Composition	Ch	Ni	Mn	N	S	C	Si	P
	Percent (wt.%)	18	8	2	0.10	0.03	0.08	0.75	0.045
	Mechanical Properties								
	Tensile Strength [MPa]	Yield Strength [MPa]	Elongation (50mm, %)	Elastic Modulus [GPa]	Hardness Rockwell B. [HR. B]				
	515 - 720	205 - 290	40 - 55	193	82 - 92				
LSP Processing Parameters									
Code	Power Density (GW/cm ²)	Beam size [mm]	Pulse area [mm ²]	Pulse energy [J]	Mass [g]				
Reference	-	-	-	-	168.773				
S/3/3	3.93	2.45	6.0025	3.3	168.513				
S/6/3	8.10	2.1	4.41	5.0	168.854				

4 RESULTS

This chapter describes the results obtained from erosion tests by giving a short-observed account of the evolution of cavitation erosion. The evolution results are given in *section 4.1* by the appearance of the samples before and after erosion test. In *section 4.2*, the cumulative volume loss and volume loss rates of each sample are shown. The surface profiles from the confocal microscope and profilometer are given in *section 4.3*. The results of each sample are color-coded with the same color for each graph. Reference sample is assigned red and blue and green for S/3/ and S/6/3 respectively.

4.1 SAMPLE PHOTOGRAPHS

Photographs the sample was taken at the onset at the onset of the test, at the end of the incubation period and at the end of the final test time for the samples. The initial surface of the sample shows a mirror polishing of the steel. This is fully depicted in

FIGURE 4-1 with a final appearance in the subsequent erosion tests.

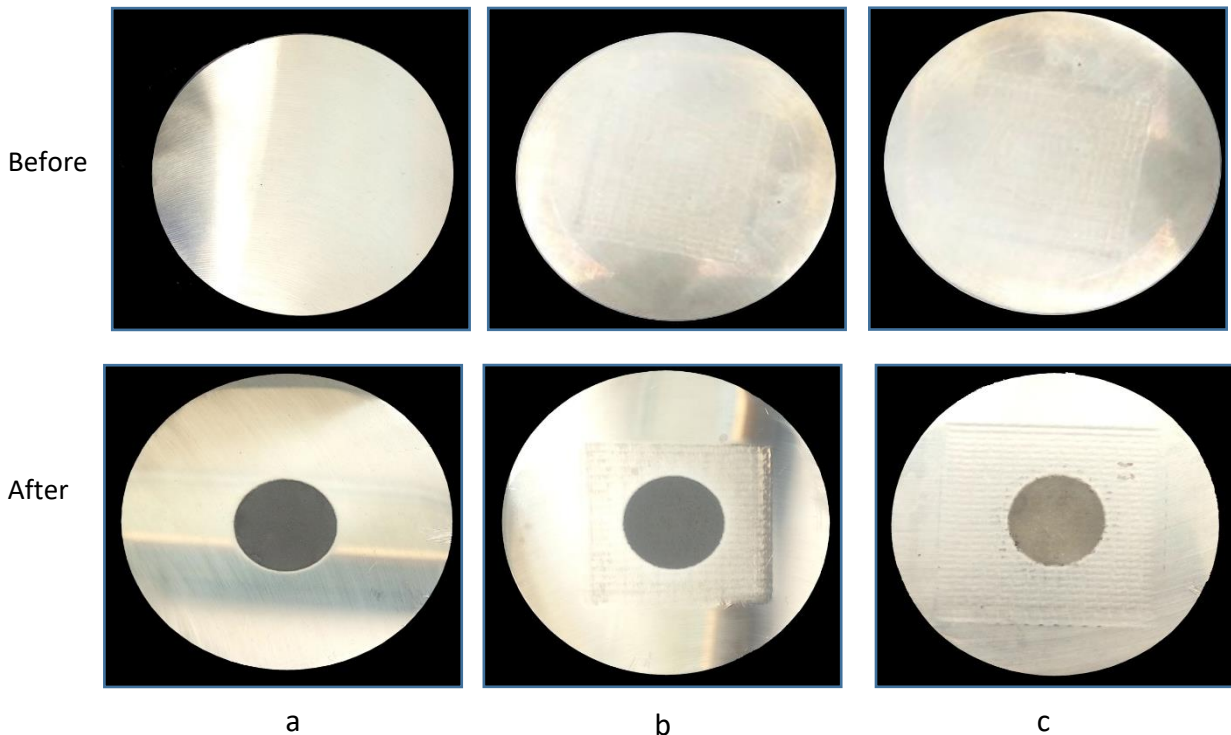


Figure 4-1. Photographs of samples of cavitation erosion (a) reference (b) S/3/3 and (c) S/6/3

The cavitation erosion zone was fully evident at the end of the incubation period for all samples. No significant changes were observed in the appearance of the zones during the acceleration period, although erosion advances with significant mass loss. The observable changes at the end of the experiments were the complete change in texture compared to the initial polished surface. The LSP treated sample showed a similar appearance to the untreated sample.

4.2 CUMULATIVE VOLUME LOSS AND VOLUME RATE LOSS

The cumulative mass loss was obtained from mass loss measured after each test interval and mass loss rates were calculated using the equations described in *section 2.5.2.3*. The results obtained were converted to volume loss using their respective density of the sample material. The volume loss rates were also computed from the mass loss rates. The results of the erosion progression through volume loss and volume loss rates are shown in *Figure 4-2* and *Figure 4-3* for individual samples depicting the stages in the erosion evolution. The erosion rates after the incubation period were fitted with a polynomial of the 9th order and compared together.

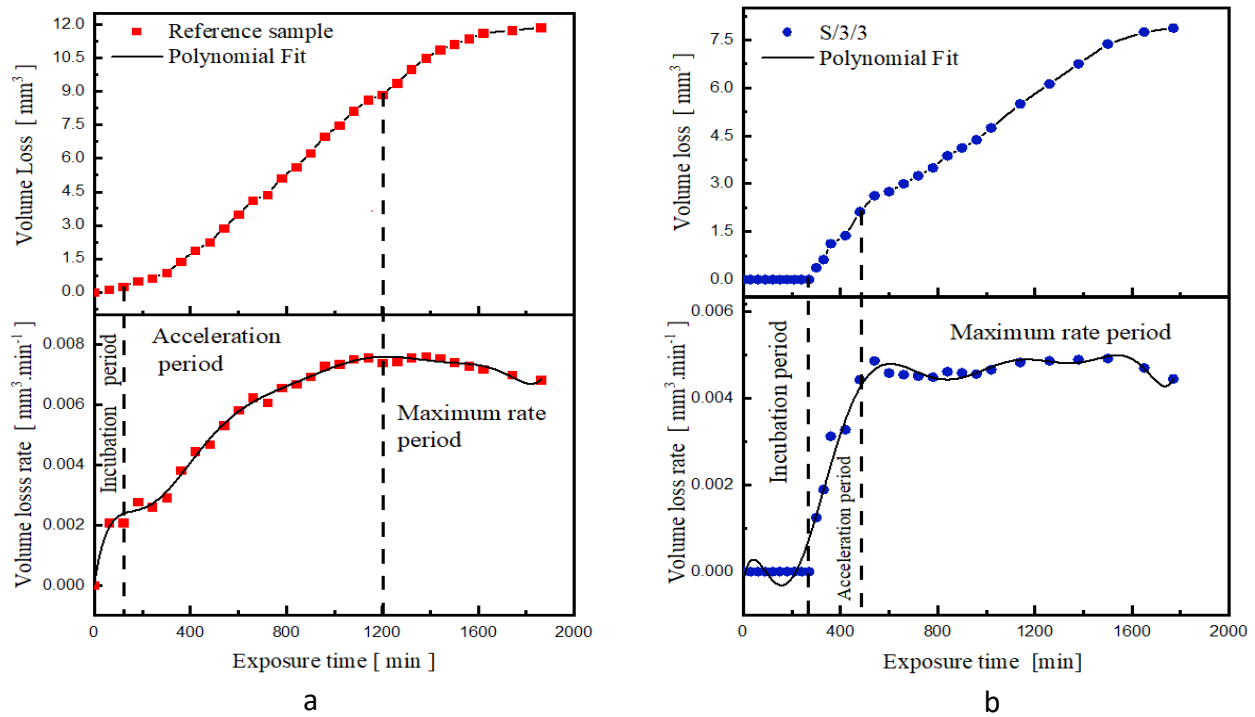
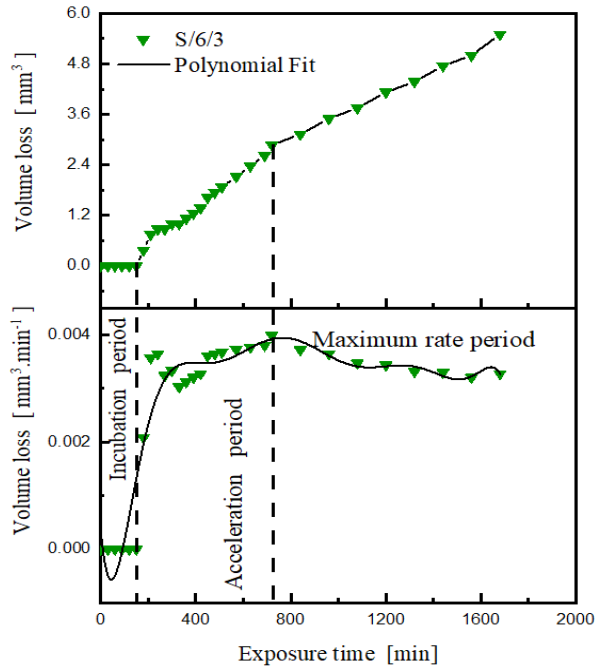
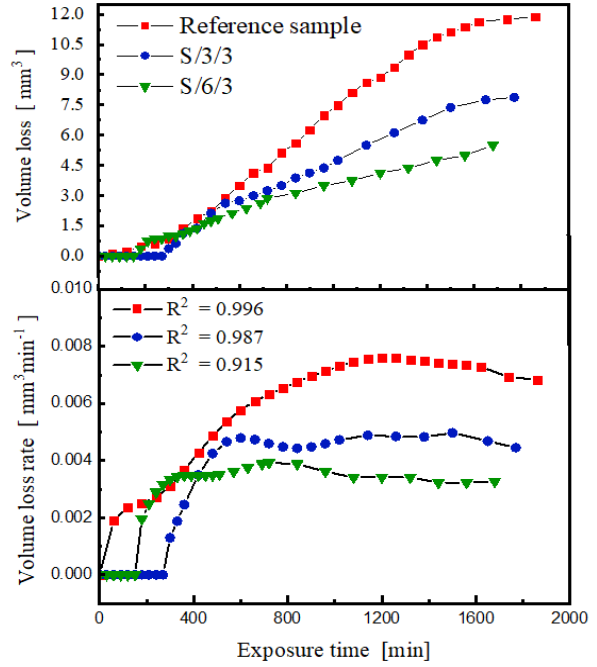


Figure 4-2. Volume loss and rates as a function of exposure time, (a) reference and (b) S/3/3



c



d

Figure 4-3. Volume loss and rates as a function of exposure time, (c) S/6/3 and (d) all samples

The results from volume loss and volume loss rate curves showed a clear distinct erosion stage for the individual samples. After a time of 60 minutes, the reference sample was observed to reach the end of the incubation period while the treated samples; S/3/3 and S/6/3 took a time of 270 and 150 minutes to attain this period respectively. The longest acceleration period was observed from the reference sample to be 1080 minutes with approximately cumulative volume loss of 8.88 mm³. The treated sample S/3/3 measured a total volume loss of 2.13 mm³ within the shortest time interval of 180 minutes in accelerating. The acceleration period for S/6/3 was distinctive by two peaks within a time interval of 540 minutes for a total volume loss of 2.88 mm³. These peaks could be attributed to the variation in the sensitivity of the weighing equipment. The erosion rates were observed to stabilize at values close to or slightly lower than the maximum value for all samples. During the steady-state stage, the treated sample S/3/3 was observed to depict a longer time before reaching a likely decelerating phase while the reference and treated sample S/6/3 would likely decelerate in advance due to observable steady-state period. The total volume loss assumed by the samples under the exposure times of the experiment is 11.88 mm³, 7.88 mm³, and 5.50 mm³ for reference, s/3/3, and S/6/3 samples respectively.

4.3 SURFACE EROSION PROFILES

In the results presented in section 4.2, the volume loss data represent a total volume loss by cavitation over the exposed area although the impact and erosion are not uniform. This considers an average depth of erosion and eliminates the information on the local depth and erosion rates. Surface roughness profile measurements can be used to provide this detail of information in addition to mass loss. It provides a convenient way of analyzing the cavitation damage and evaluating unmeasured mass loss during the incubation stage. The roughness exhibited during the incubation increases linearly. During the acceleration and maximum period, roughness increases but at a less rapid rate showing a constant rate. In this study, the profile of the samples at different times was measured with the contact profilometer for a single line *Figure 4-4*. shows the profile of the single line measurement of the depth of the samples.

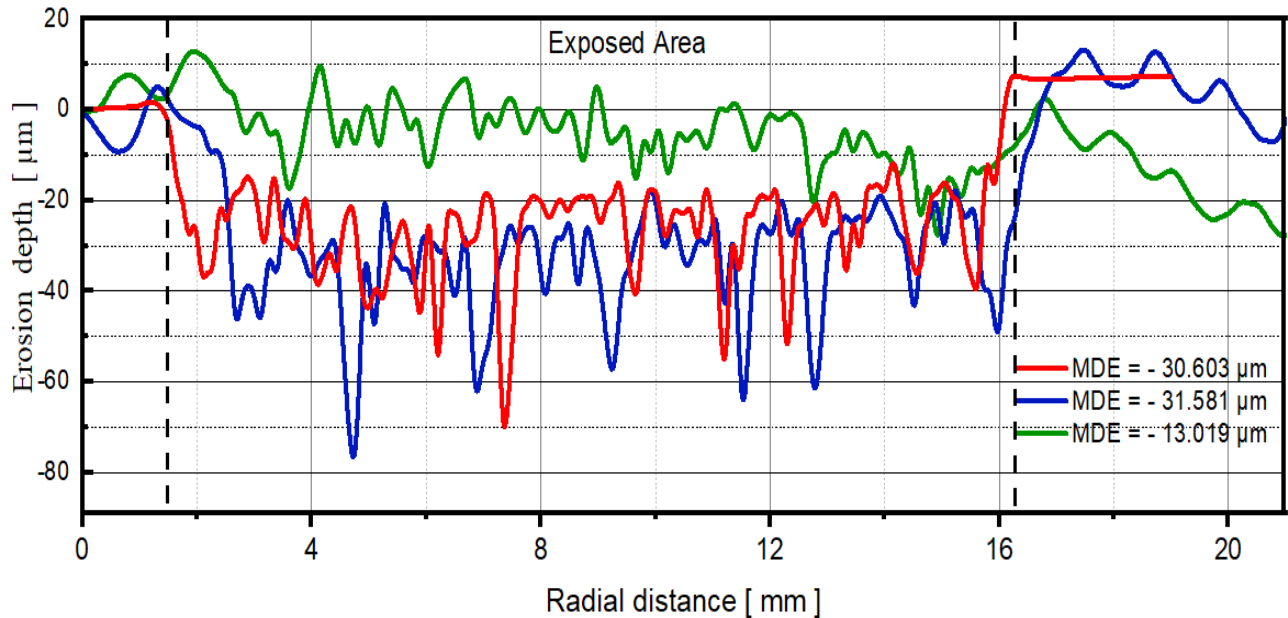


Figure 4-4. Surface profile evolution of eroded depth of samples.

The 2D profile obtained from the contact profilometry showed the depth of pits and craters in the samples. After 960 minutes it was observed that the reference sample had an average eroded depth

of 30.6 μm . This corresponds to a measured volume loss of 7.0 mm^3 from the mass loss measurement. S/3/3 was measured after 1770 minutes is showed an average depth of 31.58 μm , which corresponds to a volume loss of 7.9 mm^3 . For sample S/6/3, after 720 minutes, the average depth measured was 13.02 μm for a volume loss of 2.9 mm^3 . The single line measurement of the samples is not sufficient to conclude on the nature and magnitude of eroded depth. the results show that the treated samples had better resistances to cavitation erosion with S/6/3 having the best resistance. The eroded depth level with time is compared in figure below. This indicated that the reference sample was eroded more at lesser time compared to the time of sample S/3/3. The sample S/3/3 showed an erosion approximately 2.4 times S/6/3. This correlates with the time difference. And calculated depth from volume loss. Hence the treated samples can be assumed to realize the approximately the same level of depth for any given time.

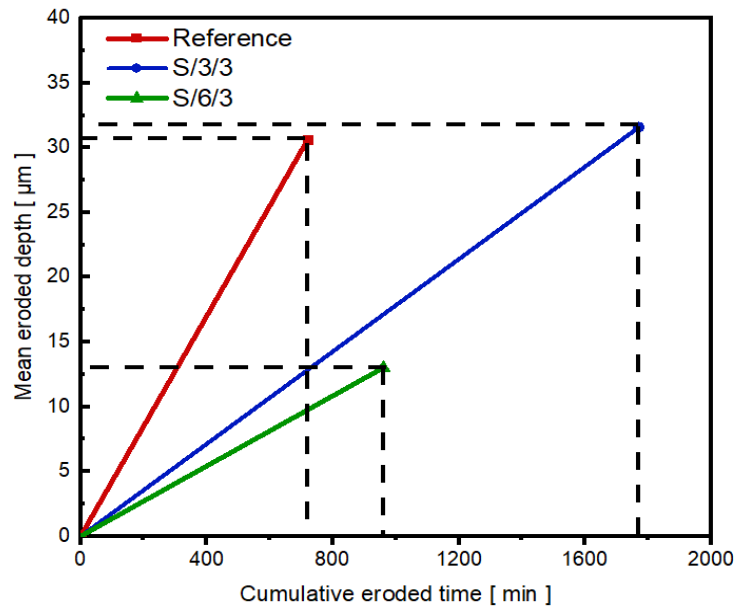


Figure 4-5. Mean eroded depth from single line measurement of profilometer

5 ANALYSIS

In this chapter, the cavitation resistances of the samples are compared in the sections. The color coding is maintained similarly from the chapter of results. The ability of a material to withstand cavitation erosion depends on the capability to absorb cavitation impacts but this does not justify a low final erosion rate. Therefore, cavitation erosion resistance is considered in two (2) ways. The initial response by incubation time and final response in the erosion stages discussed in *Section 2.5.2.2*. The volume loss and erosion depth of the test samples are discussed in *Section 5.1*. The rates of volume loss and erosion depths of the samples are also presented and discussed in *Section 5.2*. The impact of LSP treatment is presented and discussed in *Section 5.3*, to contribute to cavitation erosion and surface modification research studies, a detailed assessment of the treatment on cavitation erosion resistance.

5.1 CUMULATIVE VOLUME LOSS AND EROSION DEPTH

The volume loss and erosion depth comparison presented here provides the general idea of the material behavior in response to the cavitation field. *Figure 5-1* presents the relation of the volume loss and erosion depth of all the test samples. This showed similar curve shapes for the samples and this can be attributed to the test samples having the same composition. The observable difference in the curves was the length of the incubation period. This is due to the work hardening results from the different process parameters of the LSP treatment. The results of volume loss and erosion depth are not sufficient to describe the incubation period whose duration is not simple to define. Therefore, a nominal incubation period would be defined for this study as the cumulative time taken to reach an erosion depth of 0.7 mm. It was assumed that below this depth, mass loss was not evident due to the plastic deformation of pits. The accuracy of this definition is only valid for the material comparison purpose.

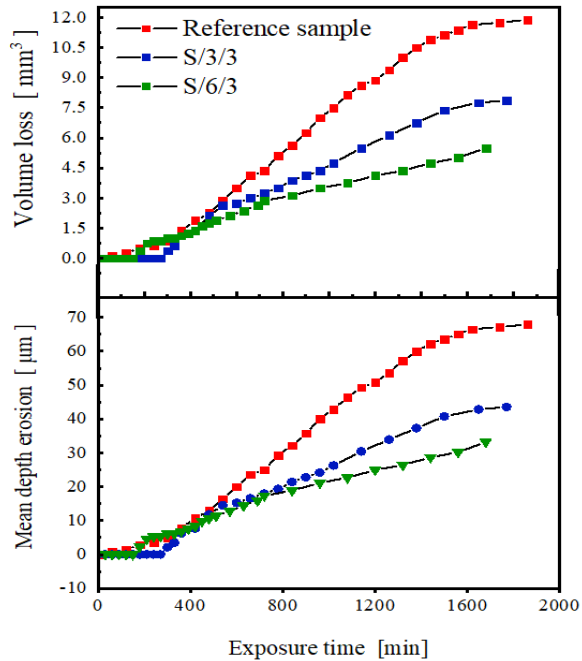


Figure 5-1. Comparison of volume loss and mean erosion depth as a function of exposure time

From the figure above, the values of mean depth erosion was proportional to the volume loss. An increasing length of the nominal incubation period can be observed for the different samples. The untreated stainless steel showed the lowest period within a cumulative time of 120 minutes. The treated sample S/3/3 showed a longer period of 300 minutes as compared to S/6/3 with a period of 180 minutes. This concludes that S/6/3 had more initial hardening and would readily undergo rapid erosion damage compared to S/3/3/. In general, the analysis of the period of incubation is used to depict the tendency of the material to undergo cavitation damage. Therefore, the indication of a long incubation period shows that material can thrive under the conditions of cavitation for a longer period without significant damage. Consequently, the reference sample would readily undergo cavitation damage within a shorter period than the treated samples. Under the conditions of this study, it can be noted that the work deformation induced by the LSP treatment anticipated the inception of the mass loss by increasing the nominal incubation time indirectly and hence delayed the onset of the maximum erosion rate.

5.2 VOLUME LOSS AND EROSION DEPTH RATES

The results of volume loss rates and erosion depth rates are present here in *Figure 5-2*. The results were also calculated using *equation 2.33* and *equation 2.35* from section 2.5.2.3. The erosion rates and depth rates depict the development of cavitation erosion beyond the incubation period. The rates compare the erosion of the materials accurately and can be used to predict the removal of deformed microstructure. Since both graphs depict the erosion rates, the results from each should fairly agree with the other. Therefore, a faster erosion depth should correspond to a faster volume loss within the same region of exposure. The interest of this comparison lies in the values of the rates for long exposure time since it reflects best on the real application for hydraulic machinery. Hence the final values of the rates are compared to the averaged final values obtained by the average of the last three (3) values of the rates. This is depicted in *Table 5-1*. This assessment determines where the material lies in the period of erosion. An acceleration period would be realized if the final rate value is significantly larger than the average value and conversely in the deceleration period for a value significantly smaller than the averaged. The steady-state is shown when the final and averaged values are close to each other. The averaging also accounts for large deviations observed as a result of large mass loss in a short period and measurement errors.

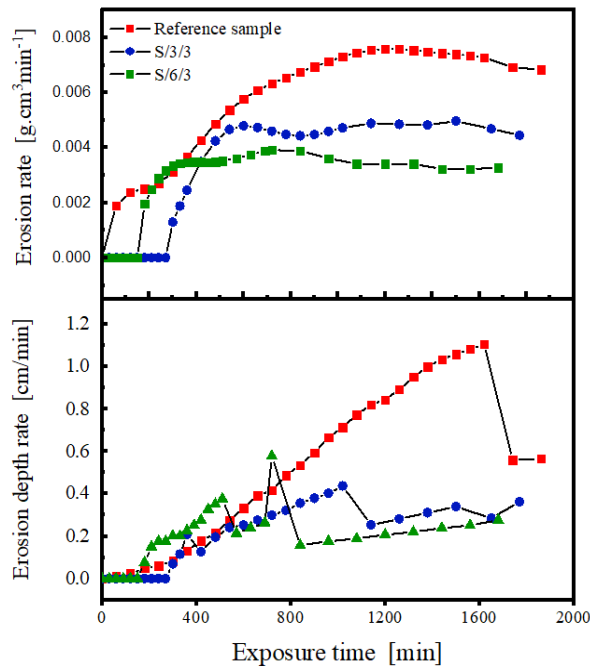


Figure 5-2. Comparison of volume loss and erosion depth rates as a function of exposure time

Table 5-1. Final and averaged values of volume loss rates and erosion depth rates of test samples.

CODE	Final Volume Loss Rates [mm ³ .min ⁻¹]	Average Volume Loss Rates [mm ³ .min ⁻¹]	Final Erosion Depth Rates [μm.min ⁻¹]	Averaged Erosion Depth Rates [μm.min ⁻¹]
Reference	0.0064	0.0068	0.57	0.74
S/3/3	0.0045	0.005	0.36	0.33
S/6/3	0.0033	0.0033	0.28	0.26

From the figure above, the MDER of the treated samples exhibited the tendency of stabilizing. This is a measure, specific to materials of high resistance to cavitation. The incubation length observed from the volume loss rates and erosion depth rates implies that the treated samples offer better resistance to cavitation erosion than the untreated sample. However, the untreated sample also offers good resistance to cavitation compared to other metals from literature, since stainless steel generally has a better quality in mechanical properties. These properties include absorption of impacts and high corrosion resistance when exposed to water, which would account for the longer incubation period of 120 minutes. As the cavitation time is increased, the number of pits formed intensifies and coalesce, leading to the formation of deep craters in the material. These craters usually represent large mass loss but also serve as dampers leading to the deceleration period. The shape of the pits or craters formed can be deduced from the erosion depth and volume loss rates. A steeper pit would be formed as is probably shown by S/6/3 sample when a higher depth rates are recorded for a lower volume loss rates as compared to the other sample. It can also be deduced from the table that; the reference sample is likely to be within the acceleration stage at the time 1800 minutes whiles the treated samples would likely lie in the early stage of the steady-state (1600 minutes).

5.3 IMPACT OF LSP TREATMENT ON CAVITATION RESISTANCE

This section presents the results of erosion depth and cumulative volume loss to define the cavitation resistance and compares to the maximum residual stress induced in the material. The compressive residual stress presented here was measured and supplied by Hilase Center after the treatment. The maximum stress of -727 MPa and -899 was achieved for S/3/3 and S/6/3 at a depth 0.05 mm respectively. the level of CRS induced in the material is usually an indicator of good cavitation erosion resistance. *Figure 5-3* compares the mean depth erosion with the residual stress after treatment. This may give an idea of the material's resistance based on a significant level of erosion. In *Figure 5-4* the cavitation resistance is clearly shown by the rates of erosion and compared to the initial resistance defined by the incubation period (IP) From that, it can be assumed that the sample with the highest resistance should take a longer time, t_{ER} to reach a specific cumulative mass or volume loss. This is depicted in *Figure 5-5* where the specific cumulative volume loss, V_L was considered as 2.8 mm^3 .

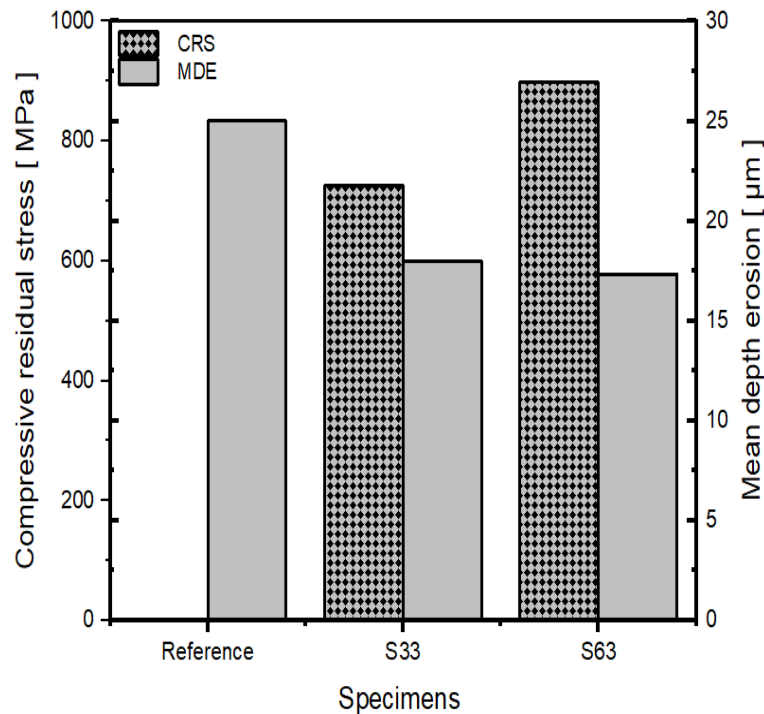


Figure 5-3. Comparison between mean depth erosion and compressive residual stress

As stated in the literature, the CRS improves the materials ability to absorb impacts from the collapsing bubbles. The material absorbs the impulse and accumulates the strains and impacts. This leads to work hardening of the surface. When cumulative strain reaches the point of rupture, the surface is easily eroded and subsequent layers are then subjected to cavitation erosion. It can be observed that both treated samples had approximately equal eroded depth. the sample with the highest induced CRS displayed a slightly less eroded depth to be 17.35 μm . Since both treated and reference samples were not eroded to a depth beyond the maximum induced CRS, it cannot be indicated that the magnitude of CRS in both samples was sufficient in improving the resistance of the material to cavitation. This occurrence can, therefore, be attributed to the good mechanical properties of the stainless steel having a homogenous distribution of the deformation with a shorter dislocation path.

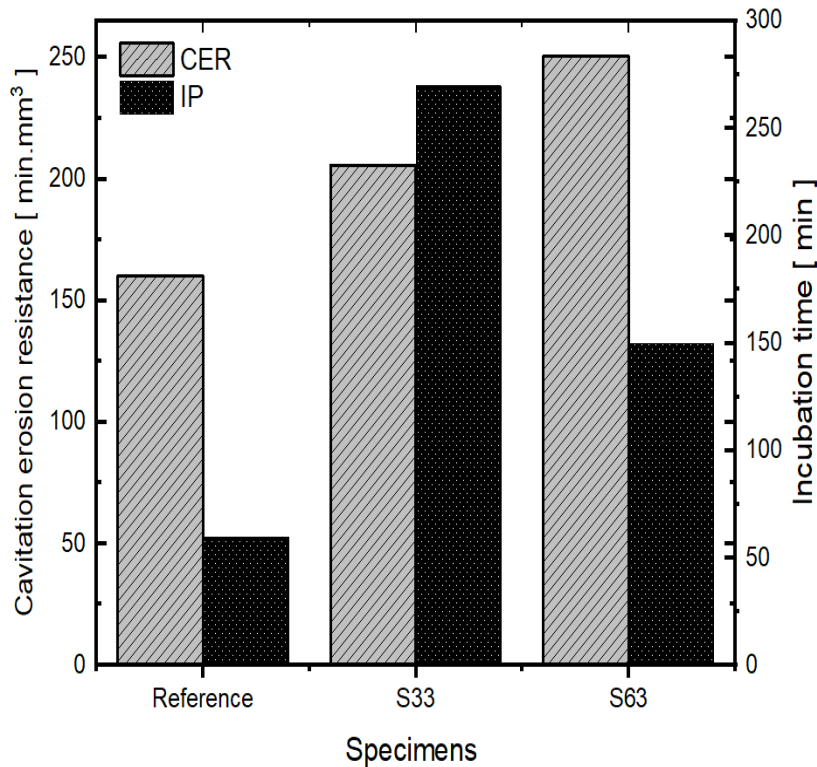


Figure 5-4. Cavitation erosion resistance and incubation period of samples.

In the case *Figure 5-4*, we considered the maximum erosion rates to describe a better picture of cavitation resistance. From literature, the cavitation resistance is defined as the reciprocal of the

maximum cumulative erosion rates. The figure above depicts S/6/3 as the specimen with the highest cavitation erosion resistance of 45.56% compared to S/3/3 and the reference which showed resistances of 32.96% and 22.48% respectively. This shows that the sample S/6/3 has a resistance approximately 2 times the reference sample. The resistances of these treated samples can be attributed to the higher power density of the treatment, which improves the material hardness as well as grain refinement. Comparing this to the incubation period (IP), it can be observed the S/3/3 had the highest initial resistance.

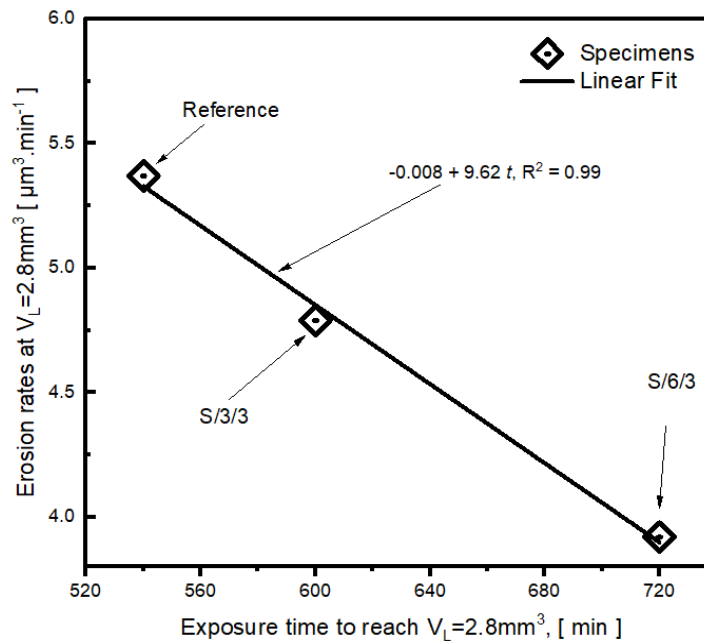


Figure 5-5. Correlation between the erosion rate and the consumed time

The relation between cavitation resistance, erosion rate and time consumed is expressed in the figure above. It affirms that the resistance of the S/6/3 is higher compared to the other samples. The time taken by reference sample to reach a volume loss of 2.8mm^3 was 540 minutes which is shorter than the 600 minutes taken by S/3/3 to erode the same volume. Considering the time taken by S/6/3 at 720 minutes and an R^2 of 0.99, a reduction in the erosion rate by a rate of $0.008\text{mm}^3 \cdot \text{min}^{-1}$ was observed. Conclusively, the treated sample S/6/3 is shown to have a good erosion resistance to cavitation.

6 CONCLUSION

This researched study was carried with a thorough literature view on the cavitation principles and surface modification technique with focus on the effect of laser shock peening technique. A brief overview of cavitation testing methods and erosion measurements was provided. The search provided a solid background on the technique and showed, simultaneously that there was limited data regarding the improvement of the cavitation erosion resistance of materials using the laser shock peening method. Therefore, the goal of this investigation was to (i) examine the cavitation erosion resistance of LSP treated steel type used for pump blades and to compare the resistance to the untreated steel type material and (ii) compare the effect of the process parameters on cavitation erosion resistance.

The experimental investigation was conducted using the vibratory apparatus with compliance to ASTM G32 recommended standards for mass loss tests. Three (3) cylindrical shaped sample of the material for pump blades was exposed to ultrasonic pressure pulse in the vibratory apparatus. The samples were exposed to different cavitation exposure times. For every test, the mass loss was recorded and evaluated as the volume loss. The mean depth of erosion was calculated from the volume loss.

The results of the tests were evaluated using the evolution of volume loss and mean depth of erosion as a function of the exposure time. The surface profile of the samples was evaluated at different times using a contact profilometer to validate the values obtained from the calculated mean depth of erosion. The cavitation erosion resistance was analyzed in two stages. The incubation period and the erosion period. The former is connected to the history of work hardening of the material and shows the tendency of the material to undergo cavitation damage. And the latter is related to the erosion rates where cavitation damage was measurable through mass loss. It was determined that, all treated samples exhibited a good resistance to cavitation erosion. the sample treated with lower power density showed a good work hardening history from the treatment. The incubation time indicated that it was 1.8 times that of the sample treated with higher power density and 4.5 times the untreated sample. The results of the erosion rates showed that the sample with low power density treatment had a faster removal of mass when compared to the higher power density treated sample. At the end of 720 minutes, the total mass loss of the high-power density

treated sample was 2.8 mm^3 which was 1.5 times less than the untreated sample. the mass loss by the lower power density treated samples was 3.3 mm^3 . This showed that the sample with the higher power density treatment has better resistance to cavitation damage.

To evaluate the effect of the laser shock treatment on the cavitation erosion resistance, the maximum mean eroded depth was compared to the maximum compressive residual stress induced during the treatment. the higher density treated sample had the higher induced residual stress. The results from comparison showed after 720 minutes, both treated samples exhibited the approximately the same level of eroded depth at $17.96 \text{ }\mu\text{m}$ and $17.35 \text{ }\mu\text{m}$ for the higher and lower power density treated sample respectively. This indicated that both treatment outcome was sufficient to improve the cavitation erosion resistance. These values were compared to the untreated sample which indicated a higher eroded depth of $25 \text{ }\mu\text{m}$. the cavitation erosion resistance was evaluated with the reciprocal of the maximum erosion rates. The sample with higher power density treatment exhibited a high cavitation resistance which was 1.3 times the resistance of the lower power density treated sample and approximately twice the resistance of the untreated sample.

Consequently, it can be concluded that laser shock peening treatment of stainless steel improves the resistance of the material to cavitation erosion and damage. A higher treatment power within the application threshold is sufficient to improve against cavitation erosion greatly. However, due to the large plasticity of stainless steel, volume loss tests is not completely sufficient to indicate the material behaviour under cavitation attack. Therefore, nano-indentation tests could be performed to best evaluate the mechanical properties such as the yield stress, elastic work ratio, and microhardness against cavitation erosion.

7 REFERENCES

- [1] GOGATE, Parag R., Rajiv K. TAYAL a Aniruddha B. PANDIT. Cavitation: A technology on the horizon. *Current Science*. 2006, **91**(1), 35–46. ISSN 00113891.
- [2] BENJAMIN, T B a A T ELLIS. The Collapse of Cavitation Bubbles and the Pressures thereby Produced against Solid Boundaries. *Philosophical Transactions of the Royal Society of London. Series A, Mathematical and Physical Sciences* [online]. 1966, **260**(1110), 221–240. ISSN 0080-4614. Dostupné z: doi:10.1098/rsta.1966.0046
- [3] Pump cavitation and how to avoid it. *World Pumps* [online]. 2018, **2**(2), 34–38. ISSN 02621762. Dostupné z: doi:10.1016/s0262-1762(18)30146-9
- [4] WAN, Mingxi a Yi Feng GAIL. *Cavitation in Biomedicine* [online]. 2015. ISBN 9789401772549. Dostupné z: doi:10.1007/978-94-017-7255-6
- [5] WAN, Mingxi, Yi FENG a Gail ter HAAR. *Cavitation in Biomedicine: Principles and Techniques* [online]. 1. vyd. B.m.: Springer Netherlands, 2015. ISBN 9789401772549. Dostupné z: doi:10.1007/978-94-017-7255-6
- [6] CHAHINE, Georges L. a Chao Tsung HSIAO. Modelling cavitation erosion using fluid–material interaction simulations. *Interface Focus* [online]. 2015, **5**(5), 1–21. ISSN 20428901. Dostupné z: doi:10.1098/rsfs.2015.0016
- [7] BURAKOWSKI, Tadeusz a Tadeusz WIERCHON. Surface Engineering of Metals - Principles Equipment and Technologies. *Materials Science & Technology*. 1999, **37**(01), 61–83.
- [8] OCATIA, JI, M MORALES, C MOLPECERES, Ja PORRO, J. GRUM a M. ZUPANCIC. LASER SHOCK PROCESSING AS A METHOD FOR SURFACE PROPERTIES MODIFICATION OF METALLIC MATERIALS. *Conference Proceedings ICSP-9* [online]. 2005, (March 2015), 466–471. Dostupné z: <http://www.shotpeener.com/library/pdf/2005126.pdf>
- [9] HOLMAN, Thomas a J WEBER. Laser shock peening of medical devices. 2011, **2**(12).
- [10] MØRCH, K. A. Cavitation inception from bubble nuclei. *Interface Focus* [online]. 2015,

- 5(5), 1–13. ISSN 20428901. Dostupné z: doi:10.1098/rsfs.2015.0006
- [11] FRANC, JEAN-PIERRE a JEAN-MARIE MICHEL. *Fundamentals of Cavitation* [online]. B.m.: KLUWER ACADEMIC PUBLISHERS, 2015. ISBN 1402022336. Dostupné z: doi:10.1007/978-94-017-7255-6_1
- [12] BRENNEN, Christopher Earls. *Cavitation and bubble dynamics* [online]. B.m.: Oxford University Press, 1995. ISBN 9781107338760. Dostupné z: doi:10.1017/CBO9781107338760
- [13] LYKLEMA, Hans. Interfacial Tension: Molecular Interpretation. *Fundamentals of Interface and Colloid Science* [online]. 2000, 3(2), 2.1-2.78. Dostupné z: [https://doi.org/10.1016/S1874-5679\(00\)80005-7](https://doi.org/10.1016/S1874-5679(00)80005-7)
- [14] YUSOF, Nor Saadah Mohd, Bandar BABGI, Yousef ALGHAMDI, Mecit AKSU, Jagannathan MADHAVAN a Muthupandian ASHOKKUMAR. Physical and chemical effects of acoustic cavitation in selected ultrasonic cleaning applications. *Ultrasonics Sonochemistry* [online]. 2016, 29, 568–576. ISSN 18732828. Dostupné z: doi:10.1016/j.ultsonch.2015.06.013
- [15] WILLIAMS, P. R. a R. L. WILLIAMS. Cavitation and the tensile strength of liquids under dynamic stressing. *Molecular Physics* [online]. 2004, 102(19–20), 2091–2102. ISSN 00268976. Dostupné z: doi:10.1080/00268970412331292786
- [16] ASHOKKUMAR, Muthupandian. The characterization of acoustic cavitation bubbles - An overview. *Ultrasonics Sonochemistry* [online]. 2011, 18(4), 864–872. ISSN 13504177. Dostupné z: doi:10.1016/j.ultsonch.2010.11.016
- [17] OZONEK, Janusz. *Application of hydrodynamic cavitation in environmental engineering* [online]. 1. vyd. Lublin, Poland: CRC Press, 2012. ISBN 9780203106099. Dostupné z: doi:10.1201/b11825
- [18] BRENNEN, Christopher E. *CAVITATION AND BUBBLE DYNAMICS* [online]. 1. vyd. B.m.: Cambridge University Press, 2014. ISBN 9781107644762. Dostupné z: www.cambridge.org
- [19] SHAH, Y. T., A. B. PANDIT a V. S. MOHOLKAR. CAVITATION REACTION

- ENGINEERING. In: Dan LUSS, ed. *The Plenum Chemical Engineering*. 1. vyd. B.m.: Springer US, 1999, s. 352 / 362. ISBN 9781461371687.
- [20] YASUI, Kyuichi. *Acoustic Cavitation and Bubble Dynamics* [online]. 1. vyd. B.m.: Springer International Publishing, 2018. ISBN 978-3-319-68236-5. Dostupné z: doi:10.1007/978-3-319-68237-2
- [21] KLIMES, Mike. Understanding and avoiding pump cavitation. *Flow Control Network* [online]. 2017, 1. Dostupné z: <https://www.flowcontrolnetwork.com/pumps-motors-drives/article/15563623/understanding-and-avoiding-pump-cavitation>
- [22] MAXIME BINAMA, ALEX MUHIRWA, Emmanuel Bisengimana. Cavitation effects in centrifugal pumps- A review. *International Journal of Engineering Research and Applications (IJERA)*. 2016, **6**(5), 52–63.
- [23] Cavitation in Pumps. *The Piping Engineering World* [online]. 2018 [vid. 2019-12-17]. Dostupné z: <https://www.pipingengineer.org/centrifugal-pump-terminology/pump-cavitation/>
- [24] BRENNEN, Christopher Earls. Cavitation in medicine. *Interface Focus* [online]. 2015, **5**(5), 1–12. ISSN 20428901. Dostupné z: doi:10.1098/rsfs.2015.0022
- [25] HONG CHEN, Andrew A. BRAYMAN, Michael R. BAILEY a Thomas J. MATULA. Blood vessel rupture by cavitation. *Bone* [online]. 2006, **23**(1), 1–7. ISSN 6176321972. Dostupné z: doi:10.1038/jid.2014.371
- [26] ASHLEY, STEVEN. Warp Drive underwater. 2001, **284**(5), 70–79.
- [27] SHANG, Zhi. Numerical investigations of supercavitation around blunt bodies of submarine shape. *Applied Mathematical Modelling* [online]. 2013, **37**(20–21), 8836–8845. ISSN 0307904X. Dostupné z: doi:10.1016/j.apm.2013.04.009
- [28] ODHIAMBO, Dan a Hitoshi SOYAMA. Cavitation shotless peening for improvement of fatigue strength of carbonized steel. *International Journal of Fatigue* [online]. 2003, **25**(9–11), 1217–1222. ISSN 01421123. Dostupné z: doi:10.1016/S0142-1123(03)00121-X
- [29] STRIDE, E. P. a C. C. COUSSIOS. Cavitation and contrast: The use of bubbles in

- ultrasound imaging and therapy. *Proceedings of the Institution of Mechanical Engineers, Part H: Journal of Engineering in Medicine* [online]. 2010, **224**(2), 171–191. ISSN 09544119. Dostupné z: doi:10.1243/09544119JEIM622
- [30] SIRSI, Shashank a Mark BORDEN. Microbubble Compositions, Properties and Biomedical Applications. *PMC - NCBI* [online]. 2007, **71**, 165–169. Dostupné z: doi:10.1179/175889709X446507.Microbubble
- [31] LEIGHTON, T. G. a Robert E. APFEL. *The Acoustic Bubble* [online]. 1994. ISBN 0124419208. Dostupné z: doi:10.1121/1.410082
- [32] CARCIOCHI, Ramiro A., Leandro G. D’ALESSANDRO, Peggy VAUCHEL, María M. RODRIGUEZ, Susana M. NOLASCO a Krasimir DIMITROV. *Valorization of Agrifood By-Products by Extracting Valuable Bioactive Compounds Using Green Processes* [online]. 2017. ISBN 9780128115213. Dostupné z: doi:10.1016/b978-0-12-811521-3.00004-1
- [33] GRIESER, Franz, Pak Kon CHOI, Naoya ENOMOTO, Hisashi HARADA, Kenji OKITSU a Kyuichi YASUI. *Sonochemistry and the acoustic bubble* [online]. 1. vyd. B.m.: Elsevier, 2015. ISBN 9780128017265. Dostupné z: doi:10.1016/c2013-0-18886-1
- [34] WU, Ta Yeong, Ningqun GUO, Chee Yang TEH a Jacqueline Xiao Wen HAY. Theory and fundamentals of ultrasound. *Chemical Engineering Journal* [online]. 2013, **2**, 5–9. Dostupné z: doi:10.1007/978-94-007-5533-8
- [35] MATULA, Thomas J. Inertial cavitation and single-bubble sonoluminescence. *Philosophical Transactions of the Royal Society A: Mathematical, Physical and Engineering Sciences* [online]. 1999, **357**(1751), 225–249. ISSN 1364503X. Dostupné z: doi:10.1098/rsta.1999.0325
- [36] MATULA, Thomas J. Inertial Cavitation and Single-Bubble Sonoluminescence. *Philosophical Transactions: Mathematical, Physical and Engineering Sciences*,. 2012, **357**(1751), 225–249.
- [37] FUCHS, John. Stable vs. Transient Cavitation. *CTG Technical Blog*. 2019.
- [38] YOUNG, F. Ronald. ACOUSTIC CAVITATION. In: *CAVITATION* [online]. B.m.: iImperial College Press, 1999, s. 1–48. ISBN 1-86094-198-2. Dostupné

- z: doi:10.1142/9781848160286_0003
- [39] YASUI, Kyuichi. *Acoustic Cavitation and Bubble Dynamics* [online]. 2018. ISBN 978-3-319-68236-5. Dostupné z: doi:10.1007/978-3-319-68237-2
- [40] HARKIN, Anthony, Ali NADIM a Tasso J. KAPER. On acoustic cavitation of slightly subcritical bubbles. *Physics of Fluids* [online]. 1999, **11**(2), 274–287. ISSN 10706631. Dostupné z: doi:10.1063/1.869878
- [41] PLESSET, Milton S. a Andrea PROSPERETTI. BUBBLE DYNAMICS AND CAVITATION. *Annual Reviews Inc.* 1977, **9**, 479–508.
- [42] T. J. MASON, J. P. Lorimer. *Applied Sonochemistry: Uses of Power Ultrasound in Chemistry and Processing.* 2002. ISBN 3527302050.
- [43] DUCK, Francis A, Andrew C BAKER a Hazel C STARRITT. *Ultrasound in Medicine.* B.m.: IOP Publishing Ltd, 1998. ISBN 0 7503 0593 2.
- [44] DULAR, Matevž, Tomaž POŽAR, Jure ZEVIK a Rok PETKOVŠEK. High speed observation of damage created by a collapse of a single cavitation bubble. *Wear* [online]. 2019, **418–419**(July 2018), 13–23. ISSN 00431648. Dostupné z: doi:10.1016/j.wear.2018.11.004
- [45] VAN WIJNGAARDEN, Leen. Mechanics of collapsing cavitation bubbles. *Ultrasonics Sonochemistry* [online]. 2016, **29**(3), 524–527. ISSN 18732828. Dostupné z: doi:10.1016/j.ultsonch.2015.04.006
- [46] GUO, Ce. The Relationship between the Collapsing Cavitation Bubble and Its Microjet near a Rigid Wall under an Ultrasound Field. In: *CAVITATION* [online]. B.m.: IntechOpen, 2018, s. 13. Dostupné z: doi:http://dx.doi.org/10.5772/57353
- [47] DULAR, Matevž, Bernd BACHERT, Bernard STOFFEL a Brane ŠIROK. Relationship between cavitation structures and cavitation damage. *Wear* [online]. 2004, **257**(11), 1176–1184. ISSN 00431648. Dostupné z: doi:10.1016/j.wear.2004.08.004
- [48] MÜLLER, M., J. HUJER, M. KOTEK a P. ZIMA. Identification of collapse patterns of cavitation bubbles close to a solid wall. *EPJ Web of Conferences* [online]. 2013, **45**, 3–6.

ISSN 21016275. Dostupné z: doi:10.1051/epjconf/20134501120

- [49] LUO, Jing, Wei lin XU a Rui LI. Collapse of Cavitation Bubble near Air Bubbles. *Journal of Hydrodynamics* [online]. 2019, (7). ISSN 18780342. Dostupné z: doi:10.1007/s42241-019-0061-x
- [50] MOUSSATOV, Alexei, Christian GRANGER a Bertrand DUBUS. Cone-like bubble formation in ultrasonic cavitation field. *Ultrasonics Sonochemistry* [online]. 2003, **10**(4–5), 191–195. ISSN 13504177. Dostupné z: doi:10.1016/S1350-4177(02)00152-9
- [51] YOUNG, Ronald F. *SONOLUMINESCENCE*. 1. vyd. B.m.: CRC Press, 2004. ISBN 0849324394.
- [52] MOMMA, T. a A. LICHTAROWICZ. A study of pressures and erosion produced by collapsing cavitation. *Wear* [online]. 1995, **186–187**(PART 2), 425–436. ISSN 00431648. Dostupné z: doi:10.1016/0043-1648(95)07144-X
- [53] KWOK, C. T., F. T. CHENG a H. C. MAN. Synergistic effect of cavitation erosion and corrosion of various engineering alloys in 3.5% NaCl solution. *Materials Science and Engineering A* [online]. 2000, **290**(1–2), 145–154. ISSN 09215093. Dostupné z: doi:10.1016/S0921-5093(00)00899-6
- [54] SAMIR, Chandra Roy. *Modeling and analysis of material behavior during cavitation erosion*. B.m., 2015. b.n.
- [55] FATYUKHIN, Dmitriy Sergeevich, Ravil Islamovich NIGMETZYANOV, Juriy Mihailovich LUZNOV, Alexander Vladimirovich SINEV a Oleg Nikolaevich TRIFONOV. A study of the influence of cavitation structures on the facial layers of structural materials. *Journal of Industrial Pollution Control*. 2017, **33**(2), 1612–1616. ISSN 09702083.
- [56] BAI, Fushi, Kai Alexander SAALBACH, Liang WANG, Xiaogeng WANG a Jens TWIEFEL. Impact of time on ultrasonic cavitation peening via detection of surface plastic deformation. *Ultrasonics* [online]. 2018, **84**(3), 350–355. ISSN 0041624X. Dostupné z: doi:10.1016/j.ultras.2017.12.001
- [57] HALLING, J. *Principles of tribology*. [online]. 1978. ISBN 3804204422. Dostupné z: doi:10.1002/9781119214908

- [58] BACH, F W, K MÖHVALD, A LAARMANN a T WENZ. Modern Surface Technology. In: *Science And Technology*. 2006, s. 1–10. ISBN 9783527315321.
- [59] RICHMAN, R. H. a W. P. MCNAUGHTON. A metallurgical approach to improved cavitation-erosion resistance. *Journal of Materials Engineering and Performance* [online]. 1997, **6**(5), 633–641. ISSN 10599495. Dostupné z: doi:10.1007/s11665-997-0057-5
- [60] SCHULZE, Volker. *Modern Mechanical Surface Treatment: States, Stability, Effects* [online]. B.m.: John Wiley & Sons, 2006. ISBN 9783527313716. Dostupné z: http://www.ghbook.ir/index.php?name=فرهنگ و رسانه های نوین&option=com_dbook&task=readonline&book_id=13650&page=73&chckhashk=ED9C9491B4&Itemid=218&lang=fa&tmpl=component
- [61] CZERWINSKI, Frank. *Heat Treatment Conventional and Novel Applications* [online]. 2012. ISBN 1477-9226. Dostupné z: doi:10.1039/c2dt31079a
- [62] CZERWINSKI, Frank. Thermochemical Treatment of Metals. In: *Heat Treatment - Conventional and Novel Applications* [online]. B.m.: Research Gate, 2012, s. 74–112. Dostupné z: doi:10.5772/51566
- [63] LI, Haibin, Zhenduo CUI, Zhaoyang LI, Shengli ZHU a Xianjin YANG. Effect of gas nitriding treatment on cavitation erosion behavior of commercially pure Ti and Ti-6Al-4V alloy. *Surface and Coatings Technology* [online]. 2013, **221**(4), 29–36. ISSN 02578972. Dostupné z: doi:10.1016/j.surfcoat.2013.01.023
- [64] WANG, Bo, Shuhua SUN, Mingwei GUO, Guofeng JIN, Zean ZHOU a Wantang FU. Study on pressurized gas nitriding characteristics for steel 38CrMoAlA. *Surface and Coatings Technology* [online]. 2015, **279**, 60–64. ISSN 02578972. Dostupné z: doi:10.1016/j.surfcoat.2015.08.035
- [65] DOBRZAŃSKI, L. A., T. TAŃSKI, A. D. DOBRZAŃSKA-DANIKIEWICZ, E. JONDA, M. BONEK a A. DRYGAŁA. Structures, properties and development trends of laser-surface-treated hot-work steels, light metal alloys and polycrystalline silicon. *Laser Surface Engineering: Processes and Applications* [online]. 2014, 3–32. Dostupné z: doi:10.1016/B978-1-78242-074-3.00001-5

- [66] KARIMI, A. Cavitation erosion of austenitic stainless steel and effect of boron and nitrogen ion implantation. *Acta Metallurgica* [online]. 1989, **37**(4), 1079–1088. ISSN 00016160. Dostupné z: doi:10.1016/0001-6160(89)90104-1
- [67] PEGUET, L., B. MALKI a B. BAROUX. Influence of cold working on the pitting corrosion resistance of stainless steels. *Corrosion Science* [online]. 2007, **49**(4), 1933–1948. ISSN 0010938X. Dostupné z: doi:10.1016/j.corsci.2006.08.021
- [68] DELGADO, P., I. I. CUESTA, J. M. ALEGRE a A. DÍAZ. State of the art of Deep Rolling. *Precision Engineering* [online]. 2016, **46**, 1–10. ISSN 01416359. Dostupné z: doi:10.1016/j.precisioneng.2016.05.001
- [69] SYSTEMS, Finishing. Shot Blasting & Sandblasting: What’s the Difference? *Finishing Systems* [online]. 2019. Dostupné z: <https://www.finishingsystems.com/blog/shotblasting-sandblasting-difference/>
- [70] FEDORYSZYN, A. a P. ZYZAK. Characteristics of the outer surface layer in casts subjected to shot blasting treatment. *Archives of Metallurgy and Materials*. 2010, **55**(3), 813–818. ISSN 17333490.
- [71] SIDDAIAH, Arpith, Bo MAO, Yiliang LIAO a Pradeep L. MENEZES. Surface characterization and tribological performance of laser shock peened steel surfaces. *Surface and Coatings Technology* [online]. 2018, **351**(March), 188–197. ISSN 02578972. Dostupné z: doi:10.1016/j.surfcoat.2018.07.087
- [72] SEALY, M. P. a Y. B. GUO. Surface integrity and process mechanics of laser shock peening of novel biodegradable magnesium-calcium (Mg-Ca) alloy. *Journal of the Mechanical Behavior of Biomedical Materials* [online]. 2010, **3**(7), 488–496. ISSN 17516161. Dostupné z: doi:10.1016/j.jmbbm.2010.05.003
- [73] GILL, Amrinder, Abhishek TELANG, S. R. MANNAVA, Dong QIAN, Young Shik PYOUN, Hitoshi SOYAMA a Vijay K. VASUDEVAN. Comparison of mechanisms of advanced mechanical surface treatments in nickel-based superalloy. *Materials Science and Engineering A* [online]. 2013, **576**, 346–355. ISSN 09215093. Dostupné z: doi:10.1016/j.msea.2013.04.021

- [74] GUJBA, Abdullahi K. a Mamoun MEDRAJ. *Laser peening process and its impact on materials properties in comparison with shot peening and ultrasonic impact peening* [online]. 2014. ISBN 1514848317. Dostupné z: doi:10.3390/ma7127925
- [75] DING, K. a L. YE. *Laser shock peening Performance and process simulation* [online]. 1. vyd. B.m.: Woodhead Publishing Limited, 2006. ISBN 9781855737679. Dostupné z: http://www.ghbook.ir/index.php?name=فرهنگ و رسانه های نوین&option=com_dbook&task=readonline&book_id=13650&page=73&chckhashk=ED9C9491B4&Itemid=218&lang=fa&tmpl=component
- [76] CLAUER, Allan H. LASER SHOCK PEENING FOR FATIGUE RESISTANCE. 1395, (1996), 217–230.
- [77] MONTROSS, Charles S., Tao WEI, Lin YE, Graham CLARK a Yiu Wing MAI. Laser shock processing and its effects on microstructure and properties of metal alloys: A review. *International Journal of Fatigue* [online]. 2002, **24**(10), 1021–1036. ISSN 01421123. Dostupné z: doi:10.1016/S0142-1123(02)00022-1
- [78] GUO, Y B. Laser Shock Peening. In: *Encyclopedia of Thermal Stresses* [online]. 2014, s. 6. ISBN 9789400727397. Dostupné z: doi:10.1007/978-94-007-2739-7
- [79] MASSE, Jean Eric a Gérard BARREAU. Laser generation of stress waves in metal. *Surface and Coatings Technology* [online]. 1995, **70**(2–3), 231–234. ISSN 02578972. Dostupné z: doi:10.1016/0257-8972(95)80020-4
- [80] HONG, Zhang a Yu CHENGYE. Laser shock processing of 2024-T62 aluminum alloy. *Materials Science and Engineering A* [online]. 1998, **257**(2), 322–327. ISSN 09215093. Dostupné z: doi:10.1016/S0921-5093(98)00793-X
- [81] GUJBA, Abdullahi K. a Mamoun MEDRAJ. Laser peening process and its impact on materials properties in comparison with shot peening and ultrasonic impact peening. *Materials* [online]. 2014, **7**(12), 7925–7974. ISSN 19961944. Dostupné z: doi:10.3390/ma7127925
- [82] CELLARD, C., D. RETRAINT, M. FRANÇOIS, E. ROUHAUD a D. LE SAUNIER. Laser shock peening of Ti-17 titanium alloy: Influence of process parameters. *Materials Science*

- and Engineering A* [online]. 2012, **532**, 362–372. ISSN 09215093. Dostupné z: doi:10.1016/j.msea.2011.10.104
- [83] SALIMIANRIZI, A., E. FOROOZMEHR, M. BADROSSAMAY a H. FARROKHPOUR. Effect of Laser Shock Peening on surface properties and residual stress of Al6061-T6. *Optics and Lasers in Engineering* [online]. 2016, **77**, 112–117. ISSN 01438166. Dostupné z: doi:10.1016/j.optlaseng.2015.08.001
- [84] FABBRO, Remy. Mechanical effects induced by shock waves generated by high energy laser pulses. *ResearchGate* [online]. 2011, **1**(November 2015), 1–7. Dostupné z: doi:10.1051/jp3
- [85] GILL, Amrinder S., Abhishek TELANG a Vijay K. VASUDEVAN. Characteristics of surface layers formed on inconel 718 by laser shock peening with and without a protective coating. *Journal of Materials Processing Technology* [online]. 2015, **225**, 463–472. ISSN 09240136. Dostupné z: doi:10.1016/j.jmatprotec.2015.06.026
- [86] SHADANGI, Y., K. CHATTOPADHYAY, S. B. RAI a V. SINGH. Effect of LASER shock peening on microstructure, mechanical properties and corrosion behavior of interstitial free steel. *Surface and Coatings Technology* [online]. 2015, **280**, 216–224. ISSN 02578972. Dostupné z: doi:10.1016/j.surfcoat.2015.09.014
- [87] DEVENDRANATH RAMKUMAR, K., Shubham SINGH, Joshy Chellathu GEORGE, S. ANIRUDH, G. BRAHADEES, Sahil GOYAL, Saurabh Kumar GUPTA, C. VISHNU, N. R. SHARAN a S. KALAINATHAN. Effect of pulse density and the number of shots on hardness and tensile strength of laser shock peened, activated flux TIG welds of AISI 347. *Journal of Manufacturing Processes* [online]. 2017, **28**, 295–308. ISSN 15266125. Dostupné z: doi:10.1016/j.jmapro.2017.06.017
- [88] RAI, Arun Kumar, Ramakanta BISWAL, Ram Kishor GUPTA, Rashmi SINGH, Sanjay Kumar RAI, K. RANGANATHAN, P. GANESH, Rakesh KAUL a Kushvinder Singh BINDRA. Study on the effect of multiple laser shock peening on residual stress and microstructural changes in modified 9Cr-1Mo (P91) steel. *Surface and Coatings Technology* [online]. 2019, **358**(November 2018), 125–135. ISSN 02578972. Dostupné z: doi:10.1016/j.surfcoat.2018.11.027

- [89] LIM, Hyuntaeck, Myunghwa LEE, Pilkyu KIM a Sungho JEONG. Laser shock peening of AISI 304 stainless steel for the application to seawater desalination pump components. *Desalination and Water Treatment* [online]. 2011, **33**(1–3), 255–260. ISSN 19443986. Dostupné z: doi:10.5004/dwt.2011.2648
- [90] ZHANG, X. C., Y. K. ZHANG, J. Z. LU, F. Z. XUAN, Z. D. WANG a S. T. TU. Improvement of fatigue life of Ti-6Al-4V alloy by laser shock peening. *Materials Science and Engineering A* [online]. 2010, **527**(15), 3411–3415. ISSN 09215093. Dostupné z: doi:10.1016/j.msea.2010.01.076
- [91] TRDAN, Uroš, Juan A. PORRO, José L. OCAÑA a Janez GRUM. Laser shock peening without absorbent coating (LSPwC) effect on 3D surface topography and mechanical properties of 6082-T651 Al alloy. *Surface and Coatings Technology* [online]. 2012, **208**, 109–116. ISSN 02578972. Dostupné z: doi:10.1016/j.surfcoat.2012.08.048
- [92] TAN, Y., G. WU, J. M. YANG a T. PAN. Laser shock peening on fatigue crack growth behaviour of aluminium alloy. *Fatigue and Fracture of Engineering Materials and Structures* [online]. 2004, **27**(8), 649–656. ISSN 8756758X. Dostupné z: doi:10.1111/j.1460-2695.2004.00763.x
- [93] TONG, Z. P., X. D. REN, W. F. ZHOU, S. ADU-GYAMFI, L. CHEN, Y. X. YE, Y. P. REN, F. Z. DAI, J. D. YANG a L. LI. Effect of laser shock peening on wear behaviors of TC11 alloy at elevated temperature. *Optics and Laser Technology* [online]. 2019, **109**, 139–148. ISSN 00303992. Dostupné z: doi:10.1016/j.optlastec.2018.07.070
- [94] STANDARDS, Annual Book of ASTM. Annual Book of ASTM Standards. In: . 2010, s. 1–2. ISBN 9780803181601.
- [95] VATSH, Paras a Krishna SAHU. Testing Methods of Cavitation Erosion and the Impact of Component Material Selection on Pump Reliability. *International Journal for Scientific Research & Development*. 2017, **5**(10), 815–823.
- [96] KRELLA, A. K. a D. E. ZAKRZEWSKA. Cavitation Erosion – Phenomenon and Test Rigs. *Advances in Materials Science* [online]. 2018, **18**(2), 15–26. ISSN 2083-4799. Dostupné z: doi:10.1515/adms-2017-0028

- [97] LICHTAROWICZ, Andrzej. JET CUTTING TECHNOLOGY. *FLUID MECHANICS AND ITS APPLICATIONS* [online]. 1992, **13**(2), 1–101. Dostupné z: doi:10.1007/978-94-011-2678-6
- [98] HUTLI, Ezddin, Milos S. NEDELJKOVIC, Nenad A. RADOVIC a Attila BONYÁR. The relation between the high speed submerged cavitating jet behaviour and the cavitation erosion process. *International Journal of Multiphase Flow* [online]. 2016, **83**(7), 27–38. ISSN 03019322. Dostupné z: doi:10.1016/j.ijmultiphaseflow.2016.03.005
- [99] DA CRUZ, Juliane Ribeiro, Sérgio Luiz HENKE a Ana Sofia Clímaco Monteiro D'OLIVEIRA. Effect of cold work on cavitation resistance of an austenitic stainless steel coating. *Materials Research* [online]. 2016, **19**(5), 1033–1041. ISSN 15161439. Dostupné z: doi:10.1590/1980-5373-MR-2015-0442
- [100] YU-KANG, Zhou a F.G. HAMMITT. CAVITATION EROSION INCUBATION PERIOD. *We* [online]. 1983, **86**(2), 299–313. ISSN 1098-6596. Dostupné z: doi:10.1017/CBO9781107415324.004
- [101] YLÖNEN, Markku. *Cavitation Erosion Characterization of a Francis Turbine Runner Blade Material*. B.m., 2015. b.n.
- [102] STYKOVÁ, Janka, Miloš MÜLLER a Jan HUJER. The improvement of the surface hardness of stainless steel & aluminium alloy by ultrasonic cavitation peening. *EPJ Web of Conferences* [online]. 2017, **143**. ISSN 2100014X. Dostupné z: doi:10.1051/epjconf/201714302119
- [103] KIM, K-H., J-P. FRANC, A KARIMI, K-H. KIM, J-P. FRANC a A KARIMI. *Advanced Experimental and Numerical Techniques for Cavitation Erosion Prediction, Series Fluid Mechanics and Its Applications*. 2014. ISBN 9789401785389.

8 APPENDIX

Table 8-1. Volume loss and mean depth erosion data for reference sample

Phase Time [min]	Phase Volume Loss [mm ³]	Cumulative Volume Loss [mm ³]	Cumulative Volume Loss Rate [[mm ³ .min ⁻¹]	Mean Depth Erosion [μm]	Mean Depth Erosion Rate [μm.min ⁻¹]
0	0	0	0	0	0
60	0.125	0.125	0.002	0.715	0.012
60	0.125	0.25	0.002	1.429	0.024
60	0.25	0.5	0.003	2.858	0.048
60	0.125	0.625	0.003	3.573	0.060
60	0.25	0.875	0.003	5.002	0.083
60	0.5	1.375	0.004	7.860	0.131
60	0.5	1.875	0.004	10.718	0.179
60	0.375	2.25	0.005	12.861	0.214
60	0.625	2.875	0.005	16.434	0.274
60	0.625	3.5	0.006	20.007	0.333
60	0.625	4.125	0.006	23.579	0.393
60	0.25	4.375	0.006	25.008	0.417
60	0.75	5.125	0.007	29.295	0.488
60	0.5	5.625	0.007	32.153	0.536
60	0.625	6.25	0.007	35.726	0.595
60	0.75	7	0.007	40.013	0.667
60	0.5	7.5	0.007	42.871	0.715
60	0.625	8.125	0.008	46.444	0.774
60	0.5	8.625	0.008	49.302	0.822
60	0.25	8.875	0.007	50.731	0.846
60	0.5	9.375	0.007	53.589	0.893
60	0.625	10	0.008	57.162	0.953
60	0.5	10.5	0.008	60.020	1.000
60	0.375	10.875	0.008	62.163	1.036
60	0.25	11.125	0.007	63.592	1.060
60	0.25	11.375	0.007	65.021	1.084
60	0.25	11.625	0.007	66.450	1.108
120	0.125	11.75	0.007	67.165	0.560
120	0.125	11.875	0.006	67.879	0.566

Table 8-2. Volume loss and mean depth erosion data for S/3/3 sample

Phase Time [min]	Phase Volume Loss [mm ³]	Cumulative Volume Loss [mm ³]	Cumulative Volume Loss Rate [[mm ³ .min ⁻¹]	Mean Depth Erosion [μm]	Mean Depth Erosion Rate [μm.min ⁻¹]
0	0	0	0	0	0
30	0	0	0	0	0
60	0	0	0	0	0
90	0	0	0	0	0
120	0	0	0	0	0
150	0	0	0	0	0
180	0	0	0	0	0
210	0	0	0	0	0
240	0	0	0	0	0
270	0	0	0	0	0
300	0.375	0.375	0.001	2.072	0.069
330	0.250	0.625	0.002	3.453	0.115
360	0.500	1.125	0.003	6.216	0.207
420	0.250	1.375	0.003	7.597	0.127
480	0.750	2.125	0.004	11.741	0.196
540	0.500	2.625	0.005	14.503	0.242
600	0.125	2.75	0.005	15.194	0.253
660	0.250	3	0.005	16.575	0.276
720	0.250	3.250	0.005	17.956	0.299
780	0.250	3.5	0.004	19.338	0.322
840	0.375	3.875	0.005	21.409	0.357
900	0.250	4.125	0.005	22.791	0.380
960	0.250	4.375	0.005	24.172	0.403
1020	0.375	4.75	0.005	26.244	0.437
1140	0.750	5.5	0.005	30.388	0.253
1260	0.625	6.125	0.005	33.841	0.282
1380	0.625	6.75	0.005	37.294	0.311
1500	0.625	7.375	0.005	40.747	0.340
1650	0.375	7.75	0.005	42.819	0.285
1770	0.125	7.875	0.004	43.510	0.363

Table 8-3. Volume loss and mean depth erosion data for S/6/3 sample

Phase Time [min]	Phase Volume Loss [mm ³]	Cumulative Volume Loss [mm ³]	Cumulative Volume Loss Rate [[mm ³ .min ⁻¹]	Mean Depth Erosion [μm]	Mean Depth Erosion Rate [μm.min ⁻¹]
0	0	0	0	0	0
30	0	0	0	0	0
30	0	0	0	0	0
30	0	0	0	0	0
30	0	0	0	0	0
30	0	0	0	0	0
30	0.375	0.375	0.002	2.263	0.075
30	0.375	0.75	0.004	2.263	0.075
30	0.125	0.875	0.004	0.754	0.025
30	0.000	0.875	0.003	0.000	0.000
30	0.125	1	0.003	0.754	0.025
30	0.000	1	0.003	0.000	0.000
30	0.125	1.125	0.003	0.754	0.025
30	0.125	1.25	0.003	0.754	0.025
30	0.125	1.375	0.003	0.754	0.025
30	0.250	1.625	0.004	1.508	0.050
30	0.125	1.75	0.004	0.754	0.025
30	0.125	1.875	0.004	0.754	0.025
60	0.250	2.125	0.004	1.508	0.025
60	0.250	2.375	0.004	1.508	0.025
60	0.250	2.625	0.004	1.508	0.025
30	0.250	2.875	0.004	1.508	0.050
120	0.250	3.125	0.004	1.508	0.013
120	0.375	3.5	0.004	2.263	0.019
120	0.250	3.75	0.003	1.508	0.013
120	0.375	4.125	0.003	2.263	0.019
120	0.250	4.375	0.003	1.508	0.013
120	0.375	4.75	0.003	2.263	0.019
120	0.250	5	0.003	1.508	0.013
120	0.500	5.5	0.003	3.017	0.025